Analysis of a 3D printed electric ducted fan for high-speed flight

van Rooij, Niek E.

Award date:
2019

Technische Universiteit
Eindhoven
University of Technology

Department of Mechanical Engineering
Energy Technology group

Analysis of a 3D printed Electric Ducted Fan for high-speed flight

Master Thesis

N.E. van Rooij

Supervisors:
dr.ir. H.C. de Lange

Final version

Eindhoven, May 2019

Abstract

Team Air/e aims to design a model aircraft that is capable of breaking the Guinnes world speed record of 750 km/h using an electric propulsion system. Most suited for propelling an aircraft up to these speeds is an Electric Ducted Fan (EDF). Since there is no EDF on the market that can provide thrust at the record breaking speed a custom EDF was designed, and a low-speed prototype was produced for testing. Using an air-accelerator the EDF could be tested at forward velocities, so called dynamic testing. Test results showed that the dynamic performance of the prototype is not as expected, even at the design point. This project aimed to find the cause for the mismatch between the prediction and the measured performance.

To gain more accurate and corresponding results both the used theory as well as the measurement procedure were examined and adapted. In addition the behaviour of the 3D material was studied. The material is relatively flexible and blade deformations and vibrations were expected to influence performance. Measurements have shown that deformation and vibrations do occur, but not to the extend that they significantly influence performance.

The project continued focusing on the influence of rotor design on the thrust characteristics. To gain insight on how certain changes affect the thrust characteristics of the EDF, and how well the new theoretical model predicts these changes, 5 additional rotor designs were made. These were produced and tested. It can be concluded that the model can be used for predicting the general trend of the thrust characteristics. Also predictions of the on-design performance have improved in accuracy. However, there does still exist an significant mismatch between the predicted and measured thrust over the wider operating range of the EDF.

Finally thrust characteristics were combined with the characteristics of the motor. There are no indications that any of the new designs improve the maximum flight velocity achieved by the initial design. However using results form this project suggestions for future designs can be made.

Contents

Chapter 1

Introduction

With climate change as a major concern the environmental impact of the aviation market becomes increasingly important. The International Civil Aviation Organization (ICAO) estimates the industry to be responsible for 2% of the global emissions [17]. However besides the amount of CO2, other factors such as the height at which it is emitted and the emission of other aerosols play a role on the influence on climate change. The exact impact is yet unknown, but different reports estimate the aviation industry as a whole to be responsible for 3.5%-5% of anthropogenic climate change, including both CO2 and non-CO2 induced effects [19][12]. Although the exact impact on climate change of the industry is subject to discussion it is inevitable that it will increase, if no action is taken. This, since the amount of travelers and the fuel consumption of the industry has been rising significantly for the past years and is expected to do so for the coming years[14][1]. To reduce environmental impact of the aviation industry several agreements have been made by for example the ICAO and the European Union, that set targets for reduced CO2 and NOX emissions [8] [4]. To meet these targets, as well as fulfilling the increasing demand for air travel the technological development for significantly cleaner aircraft is required.

Team Air/e aims on the long term to contribute to the development of high speed electrically propelled passenger aircraft. A intermediate goal set by the team is to beat the world record of fastest radio controlled model aircraft, which is set at 749.2 km/h[22]. This record is set using a turbojet engine as propulsion system using kerosene as fuel. Team Air/e wants to break this record with their own custom designed aircraft using an electric propulsion system consisting out of one or multiple Electric Ducted Fans (EDF's). Figure 1.1a shows an EDF, which is classified as an axial type of flow machine.

In the run-up to the final record breaking design the team has been developing different prototypes with (theoretical) increasing top speeds up to 290 km/h [21]. For these prototypes premanufactured EDF's were bought to be installed. However, even the most powerfull EDF available, the Shubeler DS-98-DIA HST, is only able to provide thrust up to 300-350 km/h. Since there is no EDF on the market which can operate at the record breaking speed a previous project focused on the development of such an EDF[15]. This project eventually led to a prototype being produced shown in Figure 1.1b. Except for the electric engine, shaft and bolts all the components are created using SLS 3D printing.

This prototype did however not perform as expected. Mainly the thrust characteristics diverted significantly from the expectation, even at on-design performance conditions. The fundamental problem being that the decrease of thrust due to an increasing advance ratio occurred significantly faster then expected. The advance ratio is a common dimensionless parameter that describes operating conditions. It is defined as the air distance travelled in a single revolution of a propeller.

The first aim of this project is to find the cause of the difference between the measured thrust

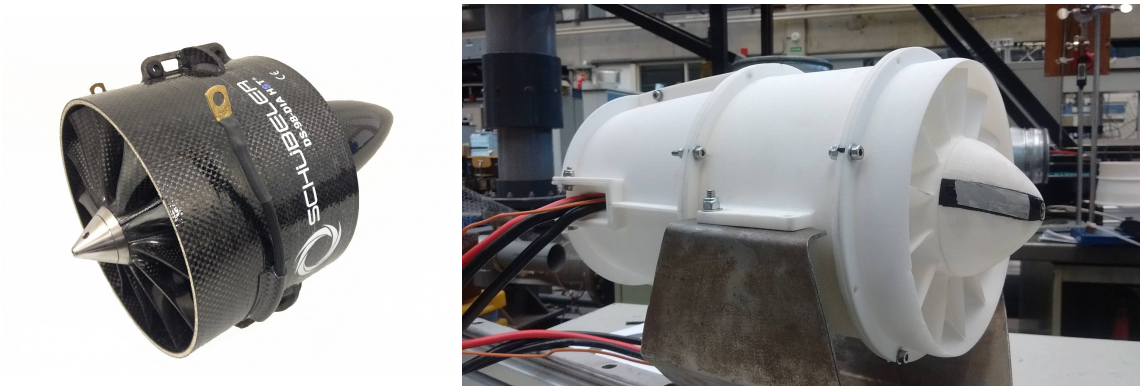

(a) Shubeler DS-98-DIA HST

(b) SLS 3D printed EDF prototype used in this project

Figure 1.1: Examples of an EDF

characteristics and the thrust characteristics predicted by the used model.

First several adaptions have been made to the setup, -shown in figure 1.2- aiming for more reliable measurement results. With these adaptions made to the setup, the measurements performed in [15] were recreated. In succession, the model, which is used in the process of designing new rotors, was revised and saw some adaptions made to the assumptions within. Additionally blade deformation and vibrations have been studied. The material is relatively flexible and the concern was that this significantly influences the thrust characteristics.

With a better understanding of the EDF's thrust characteristics 5 additional rotors were designed, produced and tested. The results have been compared with the thrust characteristics predicted by the model. The rotors focused on a specific aspect to test how a certain change influences the thrust characteristics. One of the designs aimed to achieve the on-design performance as was intended by J. van Oorschot in [15].

Finally the characteristics of the EDF with varying rotors were combined with the characteristics of the electronic motor. From this combination predictions can be made for the thrust at varying flight speeds, and how what changes to the performance are required to increase the maximum achievable flight speed.

Figure 1.2: The setup. The EDF is place in the accelerator. Figure adapted from [3]

Chapter 2

Theory

In this chapter the theory used to describe the performance of the EDF will be discussed. The first part of this chapter ,up to section 2.8, will review the equations used in the first model and the design process leading to the produced prototype done by W. Oorschot in [15]. It will also discuss the relevant results from this research in section 2.6 and 2.7.

The second part of this chapter will focus on the extension of the first model. The first model is focused on predicting performance at its design point. Section 2.8 and onward will discuss the additional parameters taken into account mainly for an improved prediction over the wider operating range.

2.1 Required EDF performance and design point

Although no detailed designs have been made of the final record breaking aircraft some estimations have been made about the required performance of the EDF for this aircraft. The turbojet engine used in the aircraft holding the current world record provides a maximum of 180 Newtons of thrust. The useful propulsive energy is the flight velocity times the thrust force, thus $208.3\dot{1}80 = 37.5kW$. Estimations of earlier projects by team Air/e estimate the required thrust to be around 250-303 N which would mean that at 750 km/h the useful power provided has to be around 52-63 kW [16][7].

The Mach number limit for the rotor tip and nozzle exit was set to 1.0. The most powerful engine found available, such that a design could be made meeting these requirements, is an Inrunner 3080 series motor with 7 windings, manufactured by Lehner Motorentechnik (LMT). This 3-phase brushless DC (BLDC) engine has a maximum power output of 27.8 kW at 41991 RPM. Combined with a flight speed of 208.3 m/s this gives the design point. One can already tell, that unless the aircraft's drag is reduced, at least 2 EDF's will be needed.

2.2 Governing equations

Added to the Mach number requirements, is the limitation that the minimum hub radius is set by the size of the electric motor. Together with the chosen design point the EDF dimensions this led to the design as shown in figure 2.1.

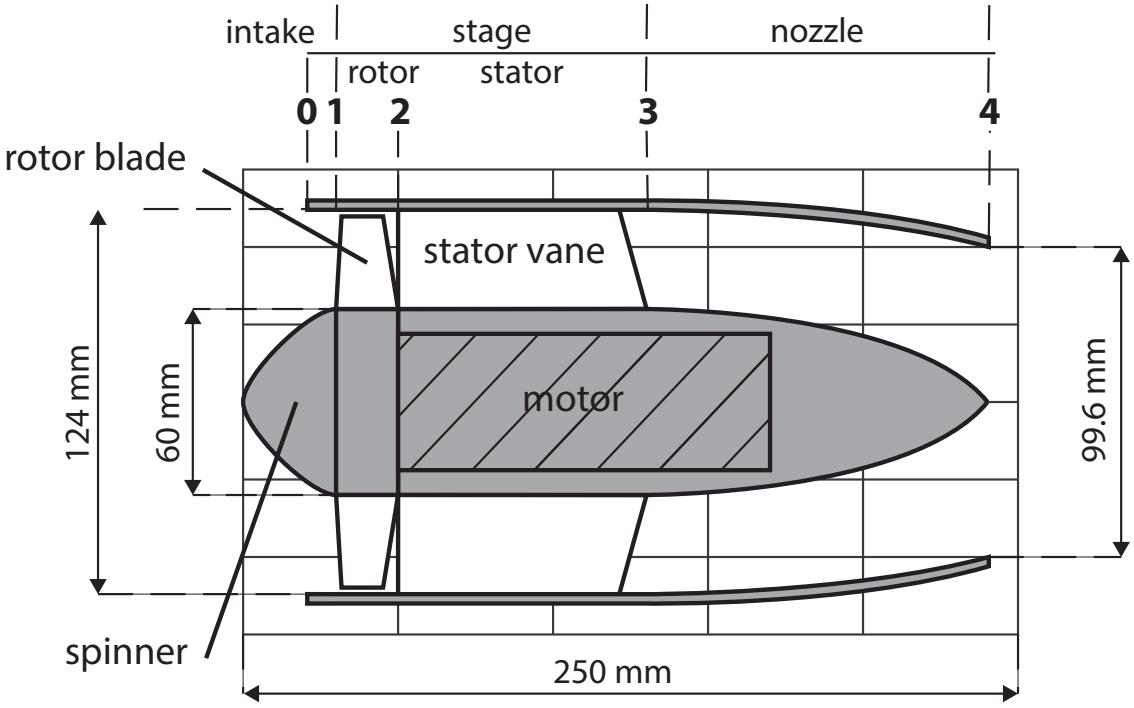

Figure 2.1: Schematic of an EDF and it's main components

The useful thrust produced by the EDF is determined using the general thrust equation 2.1:

$$F_T = \dot{m}(C_{a4} - C_{a0}) + A_4(p_4 - p_0) \tag{2.1}$$

With C_{a0} and C_{a4} the axial velocity of the air at position 0 and 4. p_0 and p_4 are the static pressures at these respective positions. $\dot{m}$ is the mass flow rate through the EDF and A_4 the surface of the nozzle exit.

Air enters the EDF at the intake. Although no work is done by the intake it is important that it allows for a disruptive free stream to the rotor of the EDF. Bad intake and spinner design can greatly influence the performance of the EDF as a whole [6]. It is assumed that the conditions at position 1 are equal to the conditions at position 0, which in turn are assumed to be atmospheric. Also the fluid velocity at position 1 is assumed to be equal to position 0, which is the flight velocity.

After the intake the fluid is accelerated by the rotor. The rotor consists out of multiple blades attached to a hub which is connected to the electric motor via a shaft. After the rotor the 4 stator vanes are placed. In contrary to the rotor blades which rotate, the stator vanes are stationary as they are attached to the casing. They recover energy by removing swirl from the flow created by the rotor and converting it to an increase in static pressure. The combination of a rotor and stator is called a stage and the total pressure increase over the stage is given by:

$$p_{03} = p_{01}\left[1 + \eta_s\left(\frac{w}{c_p T_{01}}\right)\right]^{\frac{\gamma}{\gamma-1}} \tag{2.2}$$

With T_{01} the total temperature at 1 given by:

$$T_{01} = T_1 + \frac{C_{a1}^2}{2c_p} \tag{2.3}$$

In which c_p is the coefficient of heat and γ the ratio of specific heats for air. These are assumed to be constant due to the relatively low changes in temperature and static pressure. T_1 is the temperature at position 1 and is equal to the ambient temperature which is assumed to be 293 K. C_{a1} is the axial velocity at position 1 and is equal to the flight velocity. p_{01} in equation 2.2 is given by:

$$p_{01} = p_1 \Big(\frac{T_{01}}{T_1} \Big)^{\frac{\gamma}{\gamma - 1}} \tag{2.4}$$

With p_1 the static pressure at position 1 which is assumed equal to the atmospheric pressure. This comes forward form the assumption that the conditions at position 1 are equal to that of position 0.

w in equation 2.2 is the specific work done by the rotor. This parameters is acquired via the Euler velocity triangles, see section 2.3.

η_s is the isentropic efficiency of the stage. As with the specific work more extensive calculations are required. It depends on the isentropic efficiency of the rotor and stator and how these interact. This is described in more detail in section 2.9.

Finally the air passes through a nozzle which converts the increased static pressure to increased fluid velocity. This is more efficient for propulsion purposes as for which the EDF is designed. The velocity at the nozzle exit for on-design performance is then:

$$C_{a4} = \sqrt{2 c_p (T_{03} - T_4)} \tag{2.5}$$

With T_{03} given by:

$$T_{03} = \left[\frac{w}{c_p T_{01}} + 1 \right] T_{01} \tag{2.6}$$

And T_4 by:

$$T_4 = T_{03} - \eta_j T_{03} \left[1 - \Big(\frac{1}{p_{03}/p_4} \Big)^{\frac{\gamma - 1}{\gamma}} \right] \tag{2.7}$$

With p_4 being equal to the atmospheric pressure for subsonic exit velocities. η_j is the nozzle isentropic efficiency which is assumed to be 0.95 [6].

As with the deflection and η_s, the nozzle performance also varies when the EDF is operated at off-design conditions. How this influences off-performance operation is described in section 2.11

2.3 Velocity triangles and cascade shape

In order to determine the specific work done by the rotor the Euler velocity triangles have to be solved. Figure 2.2 shows the Euler velocity triangles of the air for an axial compressor like machine at a single radius.

In which U is the tangential or radial velocity of the rotor blades given by $U_r = \omega r$. ω is the rotational speed of the rotor and r the radius from the center axis. C_a is the axial component and C_θ the tangential component of the absolute flow C. W is the relative velocity of the flow with respect to the blades. β_1 is the air inflow angle and β_2 the air outflow angle. α_1, α_2 and α_3 are the absolute flow angles.

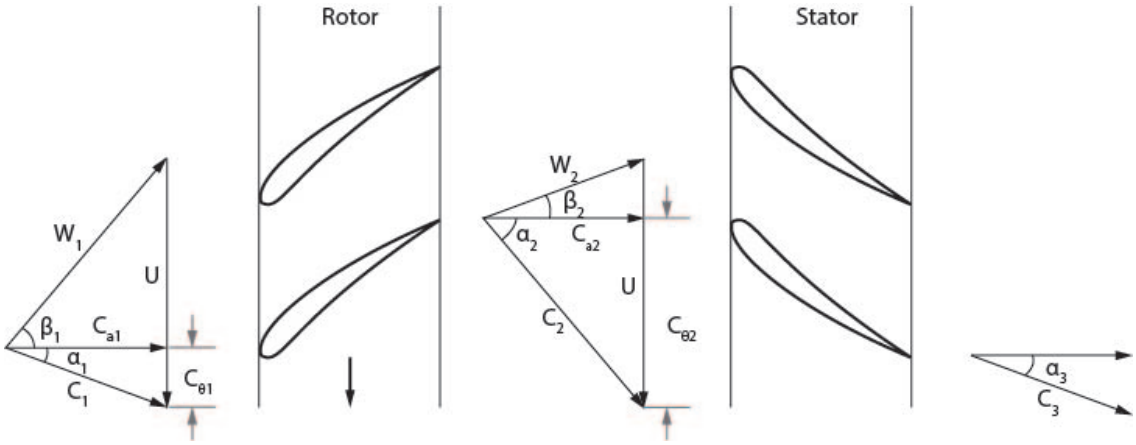

Figure 2.2: Velocity diagrams for an axial flow stage

The left triangle is solved with the assumption that the inflow is uniform and axial, thus $C_{a1} = C_1$ in which C_1 is the flight velocity. Since no tangential component is present α_1 and C_{theta1} are 0 and the air inflow angle is given by $\beta_1 = tan(U/C_{a1}$. Furthermore the design is vortex free and compressibility effects on the density are neglected. Therefore to comply with the mass balance equation $C_{a1} = C_{a2} = C_{a3}$. Besides C_{a2} and U, 1 more parameter is required to solve the second triangle. This parameter is β_2 that is retrieved using the deflection angle ϵ:

$$\epsilon = \beta_1 - \beta_2 \tag{2.8}$$

ϵ is acquired with so called carpet plots, see figure 2.6. As input it requires geometric parameters of the blade, which are acquired from [15], and the air inflow angle. Using the procedure described in 2.8 the deflection angle ϵ can now be determined. With C_{a2}, U and β_2 known the second triangle can be solved using basic trigonometry. The last 'triangle' is solved using the assumption that the stator vanes completely remove the tangential component of the absolute flow. Thus $C_3 = C_{a3}$.

The specific work can now be determined using:

$$w = U_{m2}C_{\theta 2} - U_{m1}C_{\theta 1} \tag{2.9}$$

In which U_{m1} and U_{m2} are the blade speeds in the tangential direction at the mean radius. Because the radius is equal it therefore holds that $U_{m1} = U_{m2}$. $C_{\theta 1}$ and $C_{\theta 2}$ are the tangential components of the absolute fluid velocity. With the assumption of purely axial inflow: $C_{\theta 1} = 0$. With the relation $\beta_2 = \beta_1 - \epsilon$ the specific work can now be written as function of the deflection.

$$w = U_m C_{\theta 2} = U(U - tan(\beta_2)C_{a2}) = U(U - tan(\beta_1 - \epsilon)C_{a0}) \tag{2.10}$$

In case the cascade profile is unknown and has to be designed a different approach has to be taken since one can not use the carpet plot for determining ϵ. In that case one has to determine the desired deflection ϵ at the design point depending on the available input power. This procedure is described in appendix A.

There are many more relevant angles than the air inflow and outflow angles. These will be referred to numerous times throughout this report. Figure 2.3 provides an overview of the angle nomenclature that is used in this project.

β_1 and β_2 are the air inflow and outflow angles as used before. λ is the stagger angle which is the angle between the chord line C and the axial direction. The angle between the chord and the flow

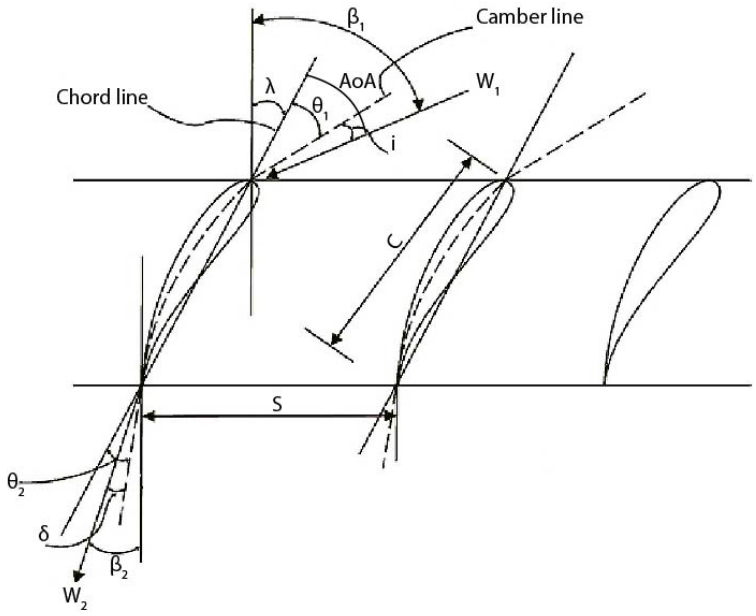

Figure 2.3: Cascade nomenclature. Figure adapted from [13]

with respect to the blade is the Angle of Attack. The angle between the Camber line and the flow is the angle of incidence i. S is the blade-to-blade space and together with the chord length C it determines the solidity σ according to $\sigma = C/S$. δ is the deviation between the actual outflow direction and the Camber line.

θ_1 and θ_2 are the angles between the Chord and Camber line at the leading and trailing edge respectively. The difference between the 2 angles is the Camber angle θ. In this project the rotor blades and stator vanes are based on NACA 65 cascades. For NACA 65 the camber angle can be retrieved via the camber, defined as C_{l0}. Using the camber the exact cascade shape and mean line are determined. From the mean line the camber angle can be retrieved.

The parameters describing blade and cascade design are used extensively throughout the project and will be referred to numerously. Therefore the values of these parameters for the rotor blades of the initial design are given in table 2.1. The parameters vary with the height of the blade. The blade is divided in 5 sections from hub to tip. The first section is at the hub radius of 30 mm, the fifth section is at the tip radius of 62 mm, see figure 2.4. The parameters for the stator vanes are given as well, see table 2.2.

	Non variable parameters				Variable angles at the design point		
Section No.	r [mm]	$\sigma[-]$	λ [°]	$C_{l0}[-]$	β_1[°]	ϵ [°]	AoA [°]
1	30	1.297	19.6	1.03	32.3	21.1	12.7
2	38	1.024	29.5	0.75	38.7	14.1	9.5
3	46	0.845	36.7	0.65	44.2	9.7	7.5
4	54	0.720	42.5	0.56	48.7	6.8	6.2
5	62	0.627	47.4	0.47	52.6	4.9	5.2

Table 2.1: Rotor blade section design parameters. Table adapted from [15]

	Non variable parameters				Variable angles at the design point		
Section No.	r [mm]	$\sigma[-]$	λ [°]	$C_{l0}[-]$	β_1[°]	ϵ [°]	AoA [°]
1	30	1.698	8.52	1.07	23.5	23.5	15.0
2	38	1.340	6.85	0.92	19.0	19.0	12.2
3	46	1.107	5.69	0.82	15.8	15.8	10.1
4	54	0.943	4.88	0.75	13.6	13.6	8.72
5	62	0.821	4.22	0.69	11.9	11.9	7.68

Table 2.2: Stator vane section design parameters. Table adapted from [15]

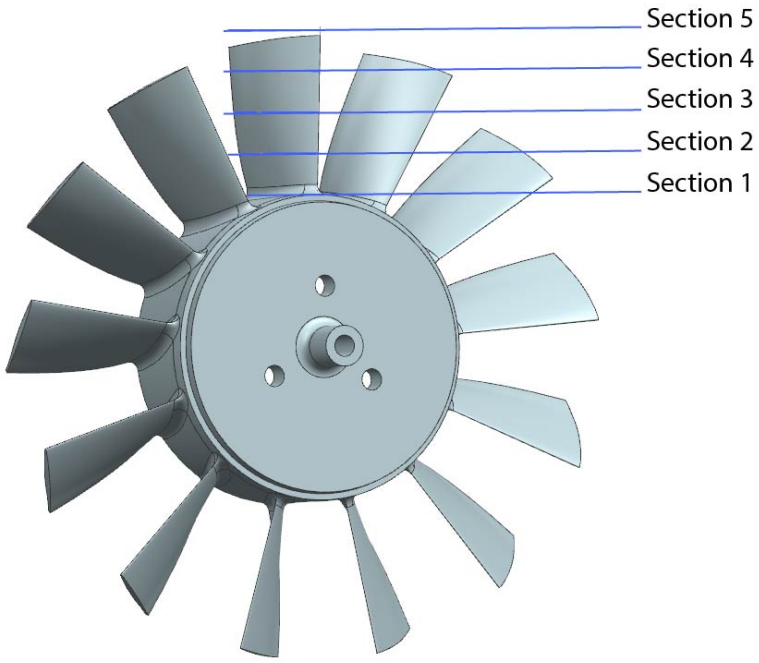

Figure 2.4: 3D CAD drawing of the reference rotor designed by J. van Oorschot

2.4 Dimensionless parameters describing performance

Important in understanding the performance of an EDF is the difference between static and dynamic thrust. Static thrust is the thrust an EDF provides when it (or the aircraft it is attached to) is stationary. Dynamic thrust is the thrust the EDF provides at different intake (or aircraft) air speeds. For this project focus will lay on the dynamic performance of the EDF.

In fluid dynamics dimensionless parameters are often used to compare small scale experimental data with theoretical results and expectations [23]. This is also the case in this project. Used are the advance ratio, thrust coefficient, power coefficient given respectively in equation 2.11-2.12.

$$J = \frac{C_{a0}}{\omega r_m} \qquad (2.11) \qquad C_F = \frac{F_T}{\rho \omega^2 r_m^4} \qquad (2.12) \qquad C_P = \frac{P_{EDF}}{\rho \omega^3 r_m^5} \qquad (2.13)$$

The advance ratio relates the rotational speed ω of the rotor blade midspan r_m to the axial fluid speed at the intake C_{a0}. In case of a high number the fluid is moving fast relative to the rotational speed of the rotor. In case of a low number the opposite is the case. There exists a relation between the advance ratio and the angle of attack which is given by equation 2.14. Since airfoils

operate within a certain range of angle of attacks the advance ratio is a useful indication whether the EDF is within operation range.

$$AoA_m = \beta_1 - \gamma = tan^{-1}(\frac{1}{J}) - \gamma \tag{2.14}$$

The thrust and power coefficient are measures of the produced thrust and the power consumption by the rotor. The definition of the thrust coefficient C_F as presented in equation 2.12 is the one most commonly found in literature. It is also used in [15] and has been adopted since the parameters used in 2.12 can be determined from measurement results.

The same holds for C_P, except that the input power of the rotor P_{EDF} can not be measured directly with the current setup. Only the power consumption of the entire powertrain can be measured, see chapter 4. Hence, in order to determine P_{EDF} the efficiencies of the electric components have to be known. This is not the case and these efficiencies can only be estimated. The system efficiency η_{system} is therefore introduced. It is defined as:

$$\eta_{system} = \frac{C_{a0}F_T}{I_{in}U_{in}} \tag{2.15}$$

With I_{in} and U_{in} the input current and voltage of the electric circuit/powertrain. Although not applicable to the theoretical model it will be used in chapter 6 to compare measurement results.

2.5 Low speed prototype

As mentioned an EDF prototype has been produced by J. van Oorschot. This prototype has the same dimensions as the intended design, it is however equipped with a weaker and cheaper engine. This is done because of multiple reasons. Firstly because the air accelerator in the setup is not able to provide a stable air flow long enough above 45-50 m/s to do reliable measurements. Therefore testing at the intended design point is only possible up to 10.4 kRPM. Secondly the electrical system in the setup can only handle currents up to 83 A. With the batteries being able to provide a maximum voltage of 48 V this results in a maximum output of nearly 4 kW. Finally there is an uncertainty in the loading the rotor blades can endure before failing. Safe operation is estimated and proven to be up to 17 kRPM.

With these limitations a LMT series 2280 inrunner BLDC motor with 10 windings has been selected for the prototype. This engine is able to provide a maximum output power of 9 kW at an input voltage of 57.6 V and running at 41 kRPM. As mentioned however it is selected to operate at much lower RPM's. At 10.4 kRPM and 14 V it delivers an estimated output power of 600 W.

2.6 Static performance

Although this project focuses on the dynamic performance of the EDF the static performance is also briefly reviewed. This allows for a useful comparison of observations. In Table 2.3 the static performance of the prototype in the current setup is compared with the theoretical expectation at a similar RPM. Also the peak performance of the Shubeler is shown as comparison.

As can be seen the results of the measurements match the theoretical expectation reasonably well. Also a more extensive comparison, done over a range of RPM's in [15] concludes that as well the measured thrust, as the measured input power show the same trend as theory predicted. Although, both quantities are over-estimated in the theoretical approach over the entire range of rotational speeds.

	Input power[kW]	kRPM	Thrust [N]
Shubeler DS-98-DIA HST (as specified)	9.7	30.5	130
Prototype (Theoretical)	1.08	13.8	25
Prototype (Measured)	0.87	13.8	23

Table 2.3: Static thrust comparison

It should be said that no conclusions should be drawn from the measured input power presented in table 2.3. Because the input power of the rotor cannot yet be determined accurately. Where the non accounted losses in thrust thus exactly originate from, cannot be said with certainty.

2.7 Dynamic performance

More relevant for this project is the dynamic performance of the EDF, especially the thrust characteristics. In this section the result of the theoretic model will be discussed by a comparison of it with previous measurement results. This comparison and the conclusions drawn from it stand at the base of the extension of the theoretic model. Performance of the EDF inside and beyond its operating range is shown in figure 2.5. Figure 2.5a shows the dimensionless input power vs the advance ratio J as theoretically predicted and as measured with the prototype. Similarly figure 2.5b shows the useful dimensionless thrust that is expected and that is measured for varying advance ratios.

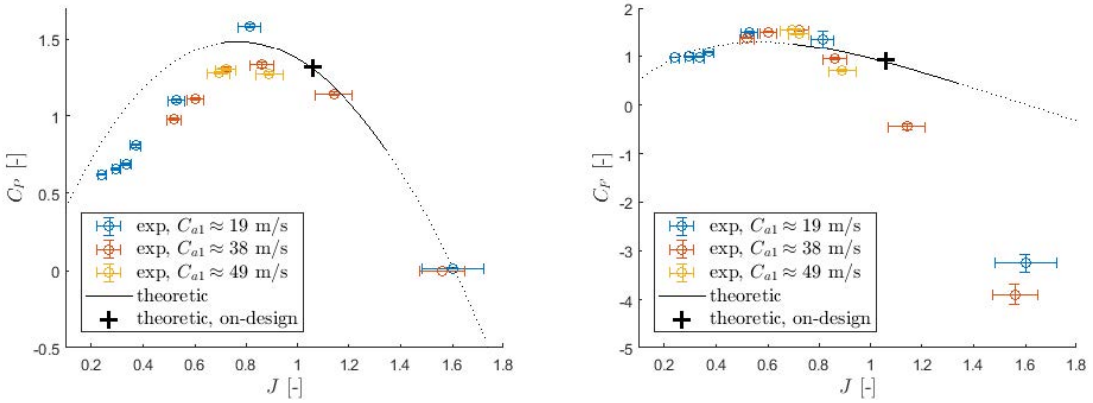

(a) The power coefficient as function of the advance ratio. The dotted part of the theoretic line denotes the operation range of the rotor in which the mid-span angle of attack is outside its efficient operation range.

(b) The thrust coefficient as function of the advance ratio. The dotted part of the theoretic line denotes the operation range of the rotor in which the mid-span angle of attack is outside its efficient operation range.

Figure 2.5: The power and thrust coefficient vs the advance ratio as measured and predicted in [15]. Figure adapted from [15]

Marked with a black cross in both figures is the design point. When the design point parameters from the design and low speed prototype design are entered in equation 2.11 one finds that the on-design advance ratio is 1.03. The theoretical produced thrust at 208.3 m/s and 42 kRPM is 95.1 N with a required power input of 27.8 kW. For the low speed prototype this is 15.1 N at a speed of 84 m/s, 17 kRPM and a rotor input power of 1.97 kW.

The theoretical prediction of the input power coefficient generally seems to over-estimate the measured input power, especially at lower advance ratios. The general trend of the data however follows that of the theoretical expectation. An explanation for the over estimation of the input

power coefficient at low advance ratios is that in this range the angles of attack are above the efficient operating range of the EDF. Therefore the actual deflection is smaller than the deflection that is expected thus requiring less power. As with the power in static conditions the estimation of the rotor input power is very rough and one should be careful in drawing conclusions with respect to the power input.

For the thrust coefficient relatively large differences between the model and the experimental data are found. For higher advance ratios, even within operation range, the thrust coefficient is much smaller than expected. However for smaller advance ratios the model seems to under estimate the performance of the EDF. No clear conclusion could be drawn what causes the difference between the model and the measurements. Possible explanations are that the performance of the EDF is influenced by the roughness and stiffness of the blades. These ideas were tested and will be discussed in more detail in chapter 5. There also seems to be an absence of stall for low values of J, although there are not enough data points to confirm this.

This chapter will continue with adaptions made to the model to improve predictability of the EDF's performance. These adaptions involve, as mentioned at the end of section 2.2, the deflection, the stage's isentropic efficiency and the nozzle performance. Eventually this extended model will be used to fabricate new rotor designs for testing.

2.8 Off performance deflection angle

As mentioned in section 2.3 the deflection angle ϵ is the difference between the air inflow angle β_1 and the air outflow angle β_2. The deflection angle is determined using a so called carpet plot for NACA 65- cascades. As input it requires the camber C_{l0}, angle of attack (AoA), solidity σ and the air inflow angle β_1. C_{l0} and σ are known from rotor design. β_1 from the Euler velocity triangles and the AoA via equation 2.14. With the carpet plot the deflection angle can be determined for as well the design point as a certain range of off-performance air inflow angles.

Using figure 2.6 (a full page version can be found in appendix B), the procedure of acquiring ϵ from the carpet plot is as follows. The entire plot contains 3 rows with 5 'carpets'. From top to bottom these rows of carpets are for camber values of $C_{l0} = 1.8$, $C_{l0} = 1.2$ and $C_{l0} = 0.4$. Each carpet is for a certain solidity, which is from left to right $\sigma = 1.5$, $\sigma = 1.25$, $\sigma = 1$, $\sigma = 0.75$ and $\sigma = 0.5$. Each carpet contains 'horizontal' lines, and 'vertical' lines. From the horizontal lines the line corresponding with the input angle of attack should be chosen. For the vertical lines this is the air inflow angle β_1. In a carpet for a certain solidity and camber one then has to find the point where the lines for the chosen AoA and β_1 intersect. From the y-axis one can now read a corresponding value of R. The relation between R and ϵ is given by equation 2.16, which originates from [5].

$$\epsilon = R - 50(Cl_0 - 0.4) \tag{2.16}$$

Direct determination of R is only possible for certain values of σ, Cl_0, AoA and β_1. For many situations interpolation is required to retrieve the value of R. For non integer values for the angle of attack and β_1 one has to interpolate within a carpet plot (see the black markers in figure 2.6. For values of σ that do not match that of the given plots one has to interpolate the points using the adjacent plots (see the green markers in figure 2.6. Similar for C_{lo}, interpolation between the rows of carpet plots is required (see the red markers in figure 2.6. This process in demonstrated in figure 2.6 for a camber value of $C_{l0} = 0.65$, $\sigma = 0.845$, AoA=4.5,8.5-14.5 and $\beta_1 = 41.2, 42.2 - 51.2$.

Interpolation of all these points is time consuming and in [15] therefore only the 2 most outer operating points, AoA=4.5/β_1 = 41.2 and AoA=14.5/β_1 = 51.2, were determined and a linear relation was adopted for the points in between. But even then, the process is time consuming and an bottleneck in the design of new rotors. Since multiple rotors had to be designed during

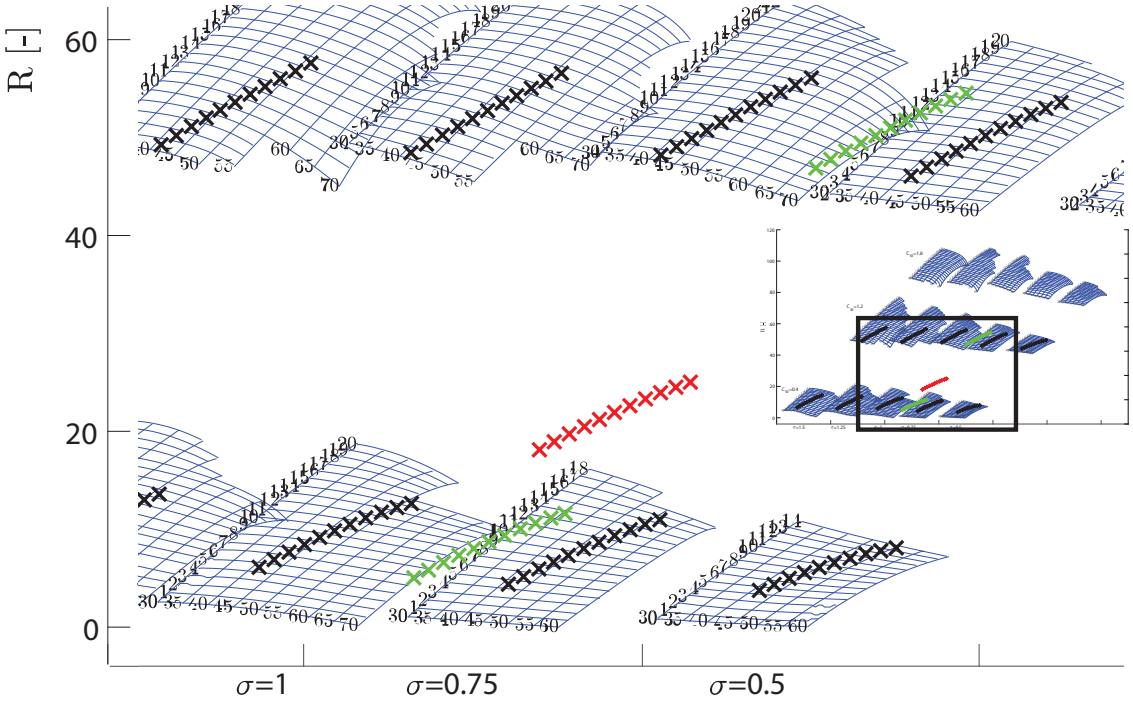

Figure 2.6: illustration of the digital carpet plot for off design performance NACA 65- series compressor blade cascades. Data within from [5].

this project, but also in future projects, the carpet plots were thus digitized. This procedure is described in appendix B.

As can be seen in figure 2.6 the points in between these 2 points are not connected by a straight/-linear line as was done earlier although the difference is marginal. More significant is however that the determination of the deflection angle is not a time consuming process anymore allowing for quicker prediction for the performance of a rotor.

2.9 Stage efficiency

The isentropic efficiency η_s used in equation 2.2 can be very well approximated by the stage efficiency η_{stage} with equation 2.17[6].

$$\eta_{stage} = \eta_{b,rotor}\Lambda_m + \eta_{b,stator}(1 - \Lambda_m) \tag{2.17}$$

In which $\eta_{b,rotor}$ and $\eta_{b,stator}$ are the rotor blade and stator vane efficiency and Λ_m is the degree of reaction at the mean radius. The degree of reaction will be described in more detail in the next chapter. The blade efficiency η_b is in turn given by:

$$\eta_b = 1 - \frac{\frac{\bar{w}}{1/2\rho V_1^2}}{\frac{\Delta p_{th}}{1/2\rho V_1^2}} \tag{2.18}$$

In this equation $\bar{w}$ is the total pressure loss and Δp_{th} is the theoretical pressure rise over the blade row. The pressure rise coefficient, which is the denominator in equation 2.18 is related to the air inflow and outflow angle via:

$$\frac{\Delta p_{th}}{1/2\rho V_1^2} = 1 - \frac{cos^2\alpha_1}{cos^2\alpha_2} \tag{2.19}$$

In which α_1 and α_2 are the air inflow and outflow angles with respect to the blade row. Which for the rotor are β_1 and β_2 and for the stator α_2 and α_3 as from the Euler triangles. The enumerator in the fraction of equation 2.18 is the loss coefficient. The loss coefficient can be determined using the following equation:

$$\frac{\bar{w}}{1/2\rho V_1^2} = \frac{C_D}{\frac{1}{\sigma}\frac{cos^3\alpha_m}{cos^2\alpha_1}} \tag{2.20}$$

With α_m the mean flow angle and C_D the overall drag coefficient, given by respectively equation 2.21 and equation 2.22.

$$\alpha_m = 1/2(tan\alpha_2 + tan\alpha_2) \tag{2.21}$$

$$C_D = C_{Dp} + C_{DA} + C_{DS} \tag{2.22}$$

C_{DA} is the annulus drag coefficient, C_{DS} is the secondary losses drag coefficient and C_{Dp} is the profile drag coefficient. The first two coefficients are determined using the following empirical relations:

$$C_{DA} = 0.020\Big(\frac{S}{H}\Big) \tag{2.23}$$

$$C_D = 0.018C_L^2 \tag{2.24}$$

With S the blade spacing and H the blade height. C_L is the section lift coefficient. C_{Dp} and C_L are determined from test data of NACA-65 cascades. This test data is from *'Systematic Two-Dimensional Cascade Tests of NACA 65-Series Compressor Blades at Low Speeds'* by L.J. Herrig, J.C.Emery and J.R. Erwin. C_{Dp} and C_L can be estimated from a series of figures of which an example is shown below:

The series of figures like figure 2.7 contain the values of various coefficients including C_{dp} and C_L versus the AoA. The experiments have been conducted for several solidities, axial inflow angles and cambers. An overview of the available tests is given in Appendix C. Test results that most closely match the design and operating conditions are used for the estimation of C_{Dp} and C_L. Using the Matlab fitting algorithm point to point fitting is performed to digitize the corresponding figures from which C_{Dp} and C_L can than be quickly extracted.

For the reference design (rotor 1) this means the used figure is that of solidity 1.00, axial inflow angle of 45 degrees and profile NACA 65-810. This since the mid span solidity is 0.845 and the range of air inflow angles varies around the design inflow angle of 44.2 degrees. The NACA 65-810 profile is chosen since it most closely matches the mid-span profile. A more detailed explanation on the NACA 65 classification of profiles will be given in section 3.3

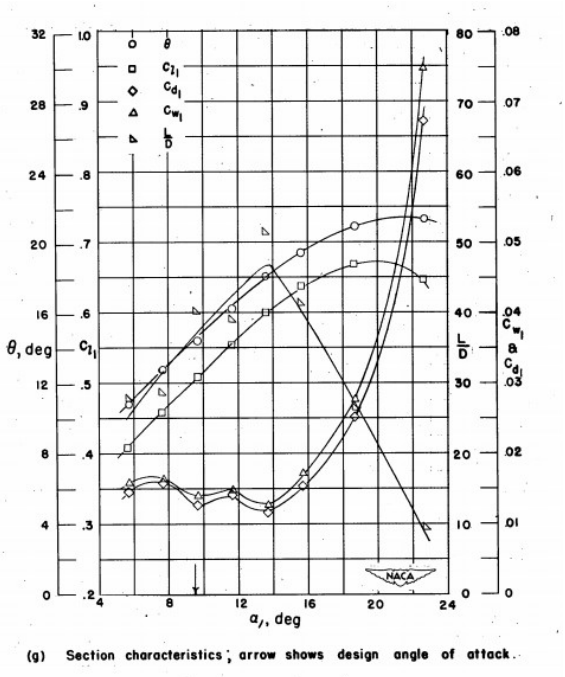

Figure 2.7: Coefficients of (profile) Drag C_{dl}, Lift C_{ll}, wake momentum C_{wl}, lift devided by drag L/D and the deflection angle θ for a blade row of NACA 65-810 cascades at a solidity of 1.00 and an angle of 45 degrees between the airflow and the axis. Figure adapted from [11]

2.10 Degree of Reaction

The degree of reaction Λ is used as a measure of the contribution of the rotor to the total static pressure rise of a stage. For uniform axial inflow conditions the following equation can be used to determine the degree of reaction Λ:

$$\Lambda = 1 - \frac{C_{\theta 2} + C_{\theta 1}}{2U} \tag{2.25}$$

For varying operating conditions all the variables on the right side of equation 2.25 are known from the Euler triangles.

The degree of reaction is an important parameter in the 3 dimensional design of the EDF. The stage of the EDF has been designed such that the 3 dimensional flow is of a vortex free design at the design point. For vortex free design the degree of reaction has to satisfy the following equation:

$$\Lambda = 1 - \frac{1}{R^2}(1 - \Lambda_m) \tag{2.26}$$

With R the radius ratio r/r_m and Λ_m the degree of reaction at the mean radius. Λ_m can be determined with equation 2.25.

As the deflection of the blades changes for varying operating conditions so does the degree of reaction. As can be seen in figure 2.8.

Seen in figure 2.8 is that the degree of reaction decreases as the angle of attack increases. This has an influence on the efficiency as can be seen in equation 2.17. Besides, it is clear that the distribution of the degree of reaction along the radius for off-performance operation deviates from

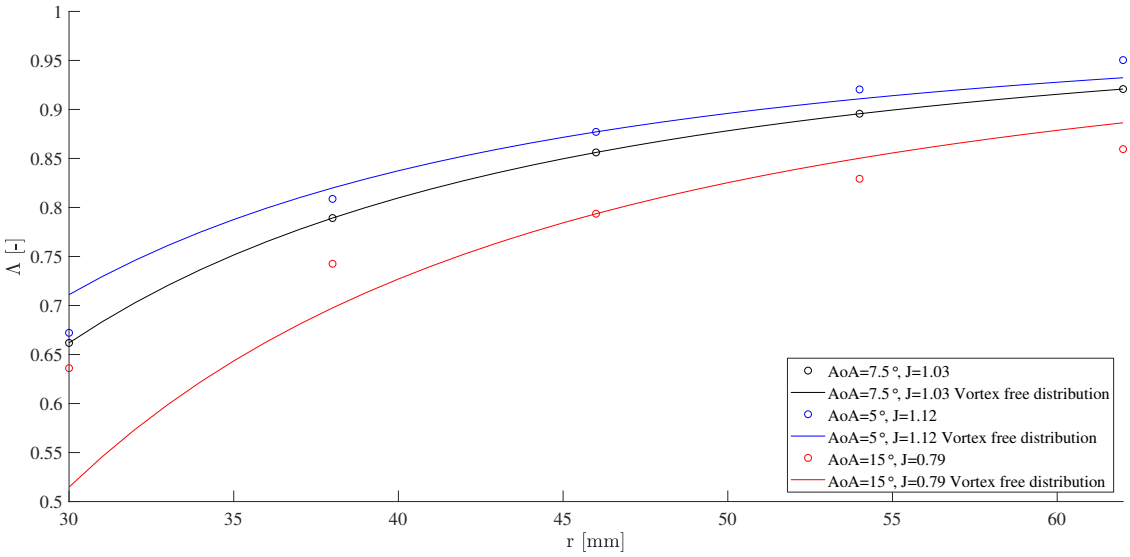

Figure 2.8: Degree of reaction vs the radius for varying operating conditions and as required for a vortex free flow.

the required distribution for vortex free flow. The exact influence of this behaviour has not been investigated further in this project but is certainly worth looking into in future projects.

2.11 Nozzle influence on off design operation

The nozzle area has a major influence on the off-design performance of a jet engine and also the EDF. Besides converging static pressure to fluid velocity it also regulates the mass flow rate. From [6] p. 397 it follows that the mass flow rate parameter is given by:

$$\dot{m}\frac{\sqrt{T_{03}}}{p_{03}} = C_4 A_4 \rho_4 \frac{\sqrt{T_{03}}}{p_{03}} = \frac{C_4}{\sqrt{T_{03}}}\frac{A_4}{R}\frac{p_4}{p_{03}}\frac{T_{03}}{T_4} \tag{2.27}$$

With the relation between pressure and velocity as given by equation 2.28. Again from [6] p. 397.

$$\frac{C_4^2}{T_{03}} = 2c_p\eta_j\left[1-\left(\frac{1}{p_{03}/p_4}\right)^{\frac{\gamma-1}{\gamma}}\right] \tag{2.28}$$

In which η_j is the nozzle efficiency that has been approximated to be 0.95 [6]. Due to subsonic outflow conditions p_4 is equal to the atmospheric pressure p_a. The ratio of p_{03} with p_a is referred to as the pressure ratio or Engine Pressure Ratio (EPR).

$$EPR = \frac{p_{03}}{p_a} \tag{2.29}$$

Substituting equation 2.28, 2.7 and 2.29 in equation 2.27 gives:

$$m = \sqrt{2c_p\eta_j\left[1-\left(\frac{1}{EPR}\right)^{\frac{\gamma-1}{\gamma}}\right]}\frac{A_4}{R}\frac{p_a}{\sqrt{T_{03}}}\left(1-\eta_j\left[1-\left(\frac{1}{EPR}\right)^{\frac{\gamma-1}{\gamma}}\right]\right) \tag{2.30}$$

A problem arises due to the fact that the conditions in the test setup is are different from normal flight conditions. All the air supplied to the EDF to the accelerator has to go through the EDF, as well that the EDF can not suck in additional air from the environment. Assuming the mass flow rate is set by the air accelerator, varying operating conditions are achieved by controlling the RPM of the EDF thus also changing the EPR. This provides a conflict with equation for off-design performance 2.30 as seen in figure 2.9.

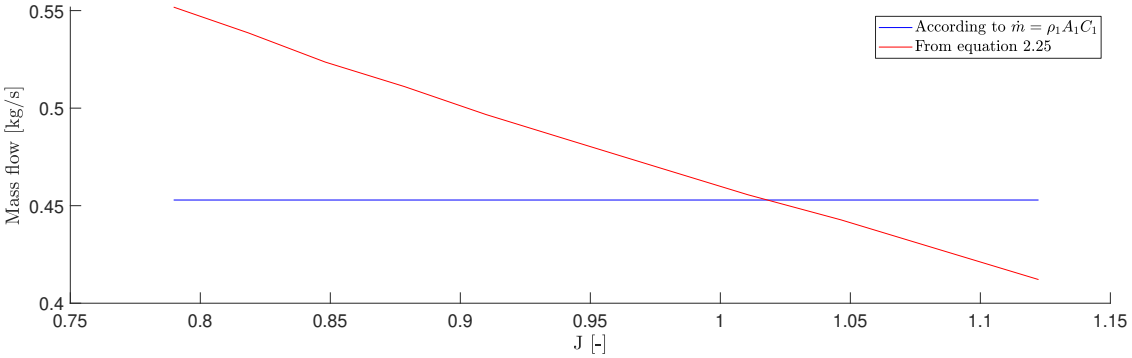

Figure 2.9: Theoretical set mass flow rate vs mass flow rate according to equation 2.25 at 40 m/s

In [6] it is stated that the nozzle influences the EPR. By matching the mass flow rate of equation 2.30 with the mass flow rate at the intake the change in EPR can be determined. For simplicity it is assumed that this change is solely caused by a change in p_1 due to the closed upstream conditions in the accelerator. The theoretical change in p_1 that is now required to match the mass flow rates is shown figure 3.1.

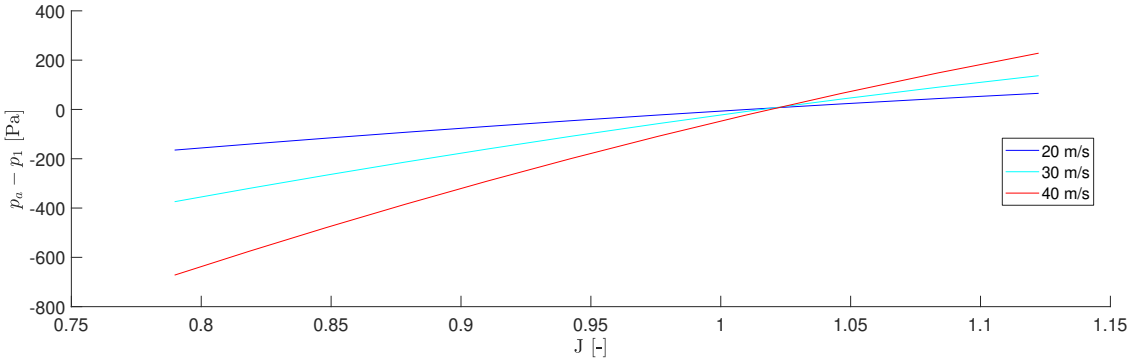

Figure 2.10: Theoretical pressure difference required at intake for matching mass flow rates

Static measurements have been conducted in front of the EDF and these results are shown in figure G.3 in appendix G. No conclusions can be drawn from this data since the measurement point was approximately 10 cm in front of the EDF. But the data does show a similar trend as the expectation presented in figure 3.1.

Chapter 3

Rotor designs

The new expanded theoretical model was used to predict the EDF performance with different rotor designs. Shown in table 3.1 is a list of the rotors that were evaluated and have also been produced and tested for a comparison. This chapter will discuss the major geometrical properties of the designs and the reasoning behind these designs.

Rotor nr.	Characteristic	main effect
Rotor 1	Reference, 13 blades	”
Rotor 2	19 Blades	increased solidity
Rotor 3	7 Blades	decreased solidity
Rotor 4	Coated	decreased surface roughness
Rotor 5	Altered thickness dist.	Smoother profile edges
Rotor 6	Decreased stagger angle	Decreased pitch

Table 3.1: Identification of different rotor designs

3.1 Variation in number of blades

Changing the number of blades will straightforward result in a variation in solidity. But how this change exactly influences performance is less straightforward and depends a lot on the design. This makes it an interesting parameter to change for comparing the theory with actual test results. From a production related aspect it is also a very easy parameter to change, since it does not require redesign of the cascades in CAD and any adoptions to the housing to be made. This would be the case if one chose to adapt the chord length. The geometric properties of the rotor sections are unchanged and thus the same as in table 2.1.

From the Carpet plots of NACA 65 profiles it can be deducted that higher solidity rotors can be operated up to higher angles of attack until $\sigma = 1.25$, provided that the air inflow angle is kept around 30-40 degrees. For solidities higher than $\sigma = 1.25$ the operating range starts to decrease again. For similar operating conditions one finds that higher solidities also result in a higher deflection angle and thus more power transferred to the fluid. Concurrent to this is the expectation that efficiency decreases with increased solidity. This is suggested by the theory in section 2.9 and test results from [2]. To ascertain to what extend these variations are true and how accurate the model can predict them, rotor 2 and 3 were created and tested. The results are discussed in chapter 6.

An important note has to made for the 3D blade design with respect to the degree of reaction. For the reference rotor the 3D blade design was tuned for vortex free design. For rotor 2 and 3

this was not the case. Table 3.2 shows how far of the degree of reaction is off at each section from the required degree of reaction for vortex free flow. These numbers hold when assumed that the flow leaves the stator vanes purely axial.

Rotor nr.	section 1	section 2	section 3	section 4	section 5
Rotor 1	0%	0%	0%	0%	0%
Rotor 2	x*	2.4%	0%	-1.5%	-0.95%
Rotor 3	2.1%	-0.62%	0%	x*	x*

Table 3.2: Difference between required and predicted degree of reaction for vortex free flow at design point (J=1.03). *these sections lie outside the performance are covered by the carpet plots

From table 3 it follows that the differences within the predictable range are only a couple percent. Due to the amount of time it takes to redesign the 3D cascade shapes and convert them to a 3D design the decision was made not to correct the cascade shapes for this effect. Since the model is only valid for free vortex designs the prediction at the design point might be off.

Finally, a table containing all of the geometrical information about rotors and cascade sections can be found in Appendix D.5. This also holds for the designs described further on in this chapter.

3.2 Coated rotor

In previous research a suggestion was made that the roughness of the rotor influences its performance. Tests done with NACA0012 cascades in [10] show that when a smoothened leading edge is used in comparison with a 'standard roughness for steel' the drag coefficient increases from 0.006 to 0.01 at an angle of attack of 0 degrees. Although no roughness numbers are known one can feel the the 3D SLS printed rotors have quite a rough surface.

Since a reserve reference rotor was available the smoother rotor was constructed by coating this rotor using varnish as recommended by the producer of the rotors. No changes were made to the geometrical properties of the rotor and these are thus the same as in table 2.1.

How this smoother rotor will exactly influence the performance has not been quantified using the model. This since the surface roughness in each case is only described qualitatively and the exact influence on the drag coefficient for the used profile is unknown. It is expected that the smoother rotor will most likely not alter the shape of curve significantly. An improvement of C_F is expected, but only slightly. This since the surface roughness should influence static performance as well, but this prediction seems to be quite accurate.

3.3 Altered thickness distribution for 3D printing

The base of this rotor design lies with a limitation of the production method. The minimum thickness of SLS printing is 0.7 mm. Therefore the cascade has to be adapted at the trailing edge where the cascade thickness drops below 0.7 mm. In the design of the reference rotor this is done by setting the thickness of the cascade to 0.7mm as soon as it drops below 0.7mm as shown below:

Shown is the originals cascade shape at the mean radius and the adapted shape that has been realised. Furthermore the mean line is shown around which a thickness distribution is defined. The combination of this mean line and the thickness distribution define the cascade shape and depend on the camber C_{l0}.

Although the major part of the profile is kept unchained there is a jump in the thickness distribution and the trailing edge profile is completely changed as seen in Figure 3.2.

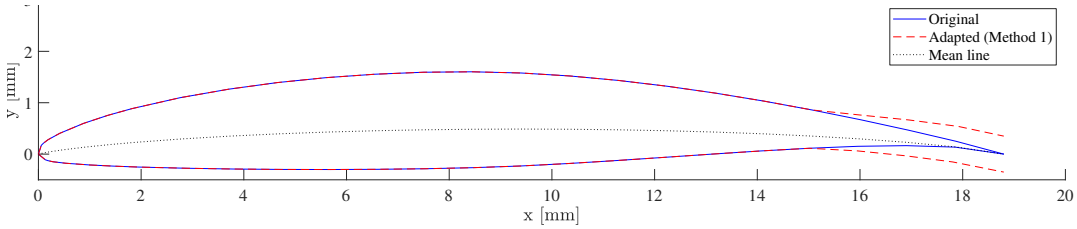

Figure 3.1: The mean radius cascade shape as originally designed versus the adapted shape for 3D printing.

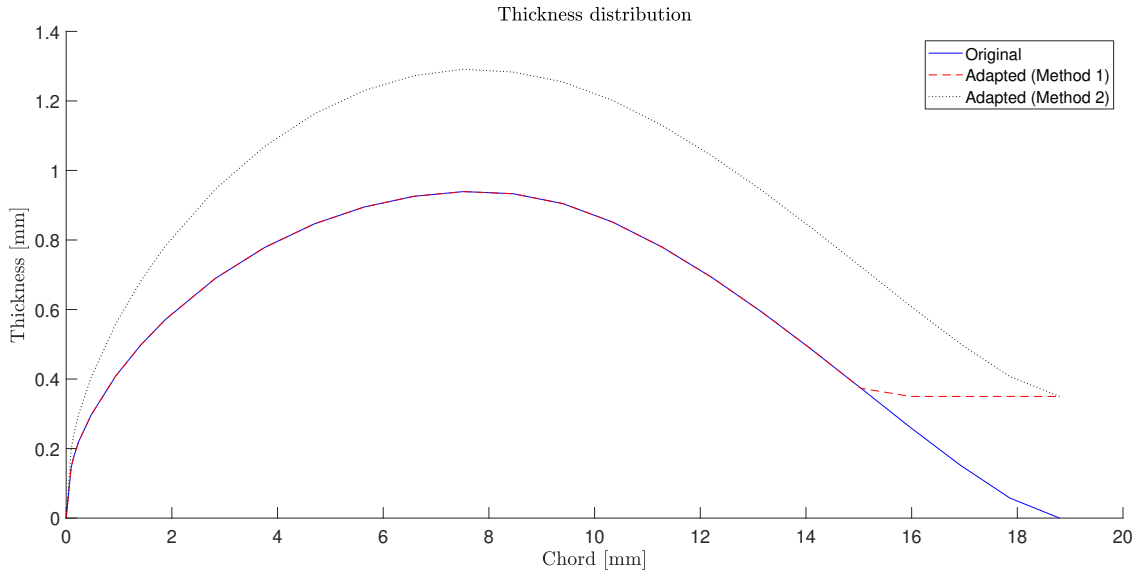

Figure 3.2: Thickness distribution at the mean radius blade section. Shown is the original distribution as a result of the design process, as adapted in the reference rotor and as adapted for rotor 5

A second difference is found in the so called lower camber angle. The lower camber angle is used to identify different variants of the NACA 65 cascades. This is important in the selection of the right figures used in determining C_L and C_{Dp} from [11]. The lower camber angle is the angle between the chord and the line tangent to the lower edge of the cascade measured from the trailing edge as shown in Figure 3.3.

For the original profile the angle is 1.45 degrees at the mean radius which shows the most resemblance with a NACA 65-810 cascade. However when method 1 is used the angle becomes -0.21 degrees and nearly a direct line can be drawn from the leading to the trailing edge. This shows more resemblance with a NACA 65 (12)/(15)10 profile which has different properties.

Therefore a different method is proposed. In order to preserve the curve of the upper and lower edge a uniform 'strip' is added of 0.7 mm. So the upper edge is moved up 0.35 mm and the lower edge moved down 0.35 mm. This method however also splits the upper and lower edge 0.7 mm at the leading edge. Therefore the leading edge is 'cut' off ,scaled in the y direction and 'pasted' to the profile. Nothing is changed to the mean line as this would change the camber angle. The thickness profile is adapted as shown in Figure 3.2. The lower edge camber angle becomes 1.46 degrees at the mean radius which is very similar to the original angle. At the other blade sections the same procedure is performed resulting in a smooth thickness distribution and a lower camber angle that better resembles the original lower camber angle as shown in the table 3.3. It is expected

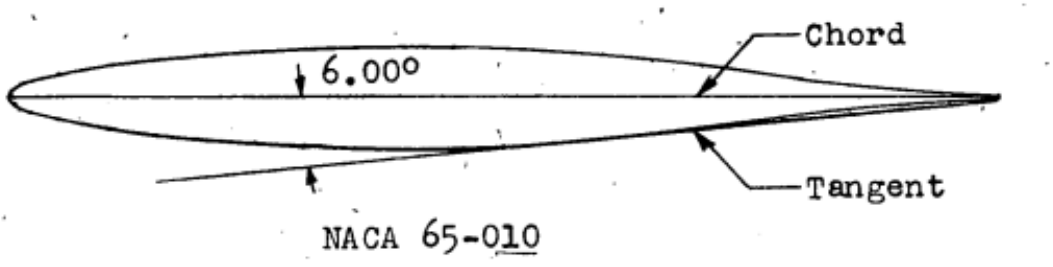

Figure 3.3: Definition of the lower camber angle. Figure adapted from [11]

that this slightly increases the thrust coefficient and increases the rotor/system efficiency.

	Original Design		Rotor 1		Rotor 5	
Section No.	θ_{lower}[deg]	Profile 65-	θ_{lower}[deg]	Profile 65-	θ_{lower}[deg]	Profile 65-
1	0.32	(12)10	-0.72	(15)10	-0.20	(12)10
2	0.94	810	-0.50	(15)10	0.92	810
3	1.45	810	-0.21	(12)10	1.46	810
4	1.98	410	0.14	(12)10	1.98	410
5	2.54	410	0.57	810	2.54	410

Table 3.3: Lower camber angles (θ_{lower}) and profiles with the most resemblance

3.4 Decreased stagger angle

In order for the EDF to achieve the intended thrust coefficient at the on-design point a rotor with a changed stagger angle was produced. The maximum power output by the motor, and thus power input of rotor, is for advance ratios J¡=1.03. Preferred is to keep the advance ratio as close as possible to J=1.03 so the tip Mach number stays minimal. From the design procedure in [15] a thrust coefficient of $C_F \approx 0.88$ was expected for J=1.03. Measurement results show however that at $C_F \approx 0.88$ occurs at J=0.95. Using relation 2.14 it is found that the angles of attack for these operation points at the mean radius are 7.5 and 10 degrees. By decreasing the mean radius stagger angle by 2.5 degrees the desired shift should be accomplished. This shift is realised by tilting the blades 2.5 degrees. It is expected that the performance of rotor 6 is similar to that of rotor 1, only shifted to a higher advance ratio region.

As with the other rotors, 3D design has to be considered. Since the entire blades are tilted the the degree of reaction is not as for a vortex free condition as with rotor 2 and 3. Table 3.4 shows how far of the degree of reaction is off at each section from the required degree of reaction for vortex free flow for rotor 6.

Rotor nr.	section 1	section 2	section 3	section 4	section 5
Rotor 6	-7.5%	-2.4%	0%	0.77 %	0.88%

Table 3.4: Difference between required and predicted degree of reaction for vortex free flow at design point (J=1.03).

Since the purpose of this rotor design is to purely test shifting of the performance curve no changes in 3D design were made. However for future designs the stagger angle could be varied over the

length of the blade to create a vortex free design. Again all the geometrical properties of rotor 6 are found in Appendix D.5.

Chapter 4

Setup and Data Acquisition

In this chapter the setup and equipment used for executing the measurements is reviewed. Also the data acquisition will be discussed.

4.1 Setup

Shown in figure 1.1a is a schematic display of the setup used in this project. Excluding the camera, it shows the default configuration for Dynamic testing.

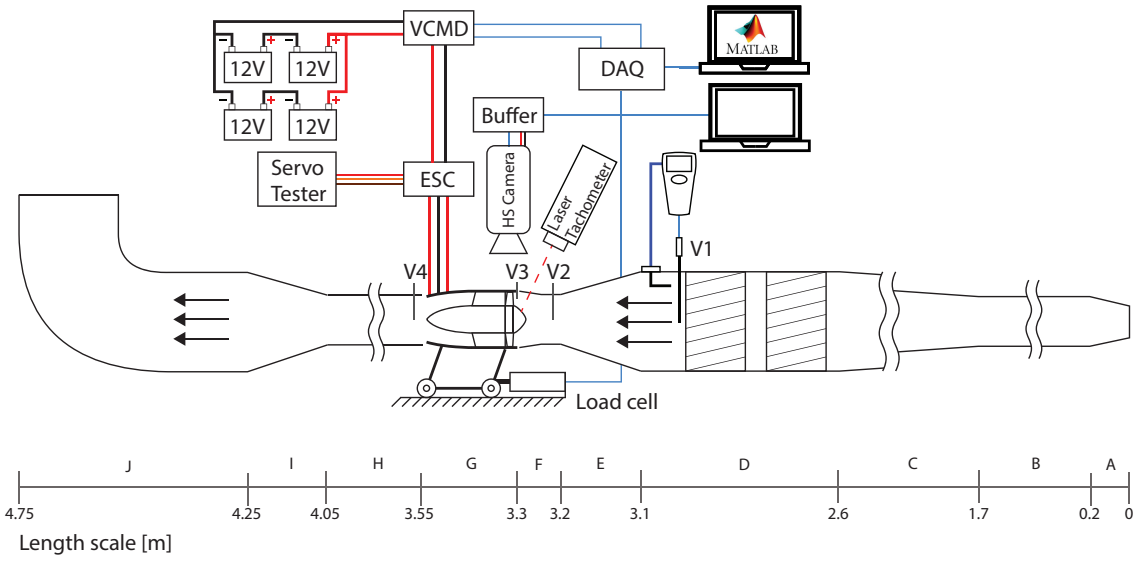

Figure 4.1

Air flows through the accelerator from right to left indicated by the arrows. Marked as section G is the EDF, that is placed in between the accelerator supply and exhaust. Power is supplied by four 12 V batteries. The VCMD measures the supplied current and voltage to the ESC. The ESC controls the rotational speed and power supplied to the engine. With the servo tester the user controls the ESC and thus the rotational speed of the engine. The laser tachometer measures the rotational speed of the rotor, the load cell the net force on the EDF and the 9565p-Multi Meter is used to measure the velocity, pressure and temperature of the air flow. Finally a high-speed camera can be installed for observation of the rotor.

4.1.1 The powertrain

With respect to older research no changes have been made to the powertrain. Power is supplied by 2 pairs of 12 V batteries being able to provide a current up to 400 A at 24 V per pair. Limiting however is the custom built VCMD (Voltage and Current Measurement Devise) that can handle currents up to 83 A and voltages up to 24 V. It uses a Hall sensor to measure the current and voltage and sends out a separate voltage signal for each of these quantities. The VCMD is placed before the ESC (Electronic speed controller) and thus measures the input of the ESC. The ESC converts the supplied DC current to a 3-phase altering current that powers the motor. By controlling the phase of the signal it controls the RPM of the engine. The ESC is in turn operated by using the Servo tester. The servo tester is controlled manually by turning an analog knob.

4.1.2 Load cell

The load cell is connected to the slide which holds the EDF and it thus measures the net force on the EDF. It gives a -10 V to 10 V signal which can be converted to the force acting on the EDF using relation 4.1. This relation has been established by calibrating the load cell with weights, see appendix H.

$$F = Offset + 50.8U_{loadcell} \tag{4.1}$$

It has to be noted that the offset voltage has to be determined for each measurement. Every time the EDF is removed, for example to switch the rotor, the offset voltage changes slightly. This has to do with the fact that the setup and slide are not completely level and there is thus a small resultant force acting on the load cell.

4.1.3 High speed camera

The cameras were installed above the EDF facing downward and focused on the tip cross section of the rotor blades. The height of the camera could be varied between 1-100 cm with respect to the blade tip.

For the optical analysis of the rotor blade behaviour 2 camera's were used. Initially a JAI GO-5000M USB was installed. This camera was readily available and easy to install due to its size. Besides the software could run on the same laptop pc as on which data acquisition was done. The camera has a resolution of 2560x2048 pixels with a corresponding frame rate of 62 fps. However a Region Of Interest (ROI) can be specified and exposure time can be set as low as 10ns so higher frame rates are possible.

Later in the project the maximum fps at which this camera can record was infsufficient and therefore a PCO 1200hs camera was installed. This camera has a resolution of 1280x1024 pixels and a corresponding frame rate of 1357 fps. As with the 5000M camera a ROI can be chosen and with the exposure time being able to be set as low as 50 ns higher frame rates are possible.

Results of both cameras are used in this project. The choice of camera, the camera settings and used lenses depended on the the measurement and will be described in more detail in chapter 5.

4.1.4 Laser Tachometer

For the RPM of the EDF a laser tachometer is used. Through a transparent section of the housing it is aimed at the spinner which has been equipped with a reflective marker. The device

can accurately measure up 99 kRPM with an error of 1 RPM. A disadvantage is, that data logging has to be done manual by noting the RPM read from the display.

4.1.5 Constant temperature anemometer and static pressure probe (Velocicalc-multimeter)

Temperature, velocity, static pressure and atmospheric pressure are measured and logged with a Velocicalc 9565-p multi-function ventilation meter produced by TSI. Logging occurs once every second although the response time for every quantity measured varies.

Velocity is measured by connecting a constant temperature anemometer probe. The constant temperature film is placed at the end of the probe at which it measures the velocity component in the direction of the film. It is therefore important that the probe is positioned correctly which is indicated by markings on the probe. It can measure velocities up to 50 m/s with a response time of 200 ms and a accuracy of $\pm 3\%$ of the reading.

Temperature can be measured with a temperature sensor present in the same probe. The sensor is however positioned 5 cm above the constant temperature film. It has a response time of 2 minutes and accuracy of $\pm 0.3°C$. The response time of the temperature sensor is slow. For measuring the temperature of the flow before it enters the EDF this is not a significant problem. A manual temperature probe shows that the temperature can be assumed to be fairly constant. However when measuring temperature behind the EDF a separate temperature probe should be used.

For the static pressure a static pressure probe is provided with the device. It can be attached easily to the exterior wall of the air accelerator. It can be submerged in the flow up to 4 cm and is connected to the multi meter with a hose. The response time of the multi meter for the pressure is 0.1 ms and the accuracy of the reading is 0.1 Pa. Finally the atmospheric pressure is measured with a sensor within the multi meter. The accuracy of these readings are $\pm 2\%$ of the reading.

V1-V4 indicate the positions at which the velocity, pressure en temperature measurements have been executed. Position V1 is the default position and in section 4.3 the choice of this position will described in more detail.

4.1.6 Air accelerator

The main components of the air accelerator are the 2 filter sections indicated by B and D, the diffusor C, the contraction E and the outlet H-J. The accelerator is fed compressed air entering the accelerator at A.

It then passes through the first filter section containing horizontal and vertical screens that intend to suppress longitudinal turbulence in order to lower turbulence intensity. The flow is than decelerated using a diffusor. This to increase the efficiency and decrease the pressure losses in filter section D. Filter section D contains filters with a honeycomb structure in order to decrease transverse and vertical turbulence in order to create a more uniform outflow.

Finally a contraction is placed before the air is fed to the EDF. This contraction converts static pressure partly to dynamic pressure. This results in a negative pressure gradient that prevents flow separation and increases flow velocity. Besides this, the flow is stabilised by flow alignment and the reduction of the turbulence intensity. After the EDF an outlet section is placed that deflects the flow upward. This to protect other equipment in the lab. An more extensive description of the functioning of the accelerator can be found in [9].

In the duration of this project a side-project aimed to improve the flow accelerator by improving the diffusor and first filter section. Mainly the uniformity of the flow was improved with deviations being reduced from 10% to 5%. A more detailed description of this process can be found in [**?**].

4.2 Data acquisition and processing

This section will discuss how the readings of the different types of equipment are processed. Data from the setup can be divided in four categories. Data gathered using the DAQ device, data gathered with the 9565-p Multi meter, data that requires manual entry and data gathered with the high speed cameras.

4.2.1 Data acquired with the DAQ

The analog voltage signals of the VCMD and load cell are sent to a NI-6211 DAQ device which in turn is connected to a laptop computer. Samples are acquired and saved by running a Simulink script written for this project. Previously a Labview script was used but due to a variety of problems this script was not used during this project.

A noticeable difference with previous research is that samples are acquired over the entire duration of the measurement run without needing further actions during the measurement as was previously the case. This way mistakes are less likely to be made and a clearer view of EDF performance is acquired.

This method does however give the complication that the signal needs to be cut up afterwards to retrieve the useful samples. Therefore an algorithm was created with Matlab that can find the useful samples as is shown in figure 4.2.

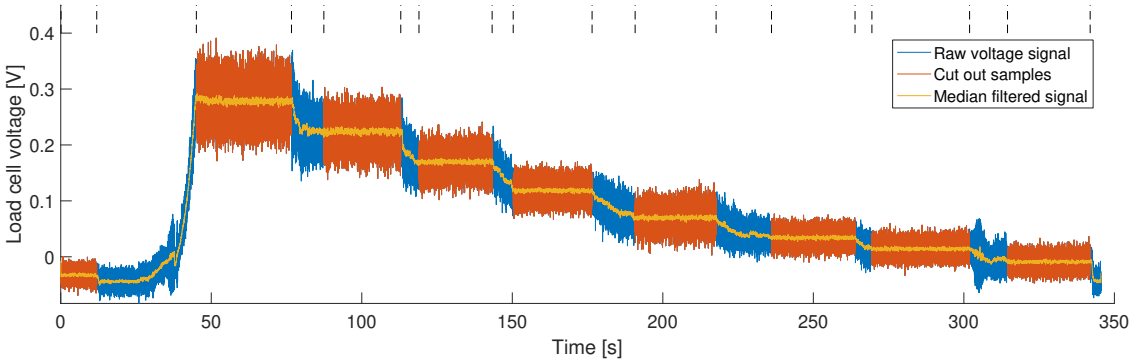

(a) Division of the voltage signal for the force in sections of steady operation

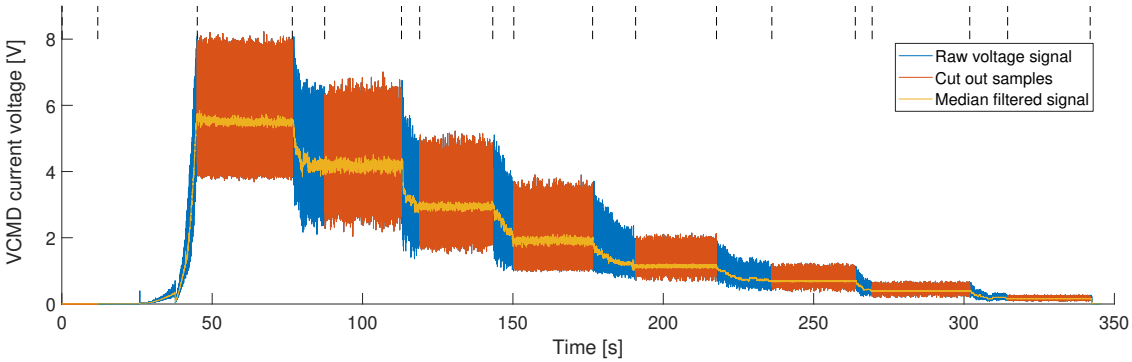

(b) Division of the voltage signal for the current in sections of steady operation

Figure 4.2: Example of the division of the raw voltage signals for run 70.

The user specifies the minimum amount consecutive samples that the script should cut out. The script applies a median filter to look for consecutive samples for which the median filtered value

lies within a certain threshold. The sample width of the filter and the value of the threshold rely on the local deviation of the samples.

It has to be said that the script is not 100% accurate and mainly sharp peaks in the data are difficult to remove. Therefore settings can be changed manually as well as that the user can add, remove or adapt sections easily. It can also be selected whether to use the load cell or current signal to create the sections. The voltage signal cannot be selected since the method described above is not applicable to this signal. This, because the voltage signal also drops when the EDF is in steady operation.

The thrust is finally acquired by inserting the voltage signal of the load cell the calibration equation 4.1. The amperage is retrieved by multiplying the voltage signal with 8.333 and the voltage by multiplying the signal for the voltage with 5.0.

4.2.2 Data acquired with the 9565p-Multi Meter

The multi meter stores the velocity, temperature, pressure and atmospheric pressure once every second. As with the DAQ sampling occurs constantly during the measurements. The multi meter can be connected to a laptop computer and with software provided by TSI the samples can be stored in .txt formats. A Matlab script was created to convert these .txt files to Matlab variables to process.

However due to the low logging rate of 1 Hz and air accelerator velocity often being set constant during a measurement it is difficult to cut out the right samples automatically as is done with the data from the DAQ. Therefore the acquisition with the multi meter is started simultaneously with the acquisition from the DAQ. This, so the timestamps from the load cell or current signal can be used to cut the logged samples from the multi meter.

4.2.3 Data acquired with the laser tachometer

The reading of the laser tachometer is shown on a display and has to be manually noted during the measurements. Since measurements at high power and/or high velocity deplete the batteries and air supply quite rapidly this allows for notation of roughly 5 readings. Due to the high accuracy of the tachometer the relative deviation of the noted samples is not considered a problem although the amount of samples are limited. Other methods that automatically log the samples have been tried out but seemed to difficult to implement or to unreliable to compete with the tachometer.

4.2.4 Data acquired with the high speed cameras

For both of the cameras that were used the captured frames were stored directly on hard drives in the form of separate images. Post processing of these images is discussed in chapter 5.

4.3 Intake velocity and mass flow rate

The axial velocity and the mass flow rate of the fluid entering the EDF are crucial parameters for expressing the performance. The mass flow rate and flow velocity are linked according to equation 4.2. Using the ideal gas law the fluid density is related to the measurable quantities temperature and static pressure. In this equation an ideal gas is assumed as well as uniform inflow conditions.

$$\dot{m} = \rho_1 A_1 C_1 = \frac{p_1}{R_{air} T_1} A_1 C_1 \tag{4.2}$$

In this equation R_{air} is the specific gas constant or air and A_1 is the through flow surface at position 1 as in 2.1. The rest of the parameters are as described in chapter 2. Due to the low velocities and the absence of a major heat source local variations in ρ_1 by local variations in p_1 and T_1 can be safely neglected. Local variations in the velocity can however not be deemed negligible. A project involving the air accelerator by R. Coolen shows that the velocity outflow profile of the accelerator varies up to 5% of the bulk or average velocity. Besides this the flow is also deflected by the spinner before it enters the stage. It can thus be said that a uniform inflow velocity can not be assumed. However since the exact influence of the spinner is yet unknown as well as the fact that a non-uniform inflow condition cannot yet be taken into account in the model it is assumed nevertheless that $C_1 = C_{1bulk}$.

In preceding research the inflow velocity, temperature and static pressure were never measured directly for obvious reasons. Firstly a pitot tube was used which was difficult to insert correctly at this location. But more importantly, inserting multiple probes in front of the rotor disrupts the intake air flow.

For this reason the intake velocity was calculated via estimating the mass flow rate at the outlet of the EDF. Due to the fact that only 1 pitot tube was available and the outflow profile of the EDF is strongly non uniform the bulk velocity had to be estimated. This method is often used when the profile of the flow is known and the velocity at the measurement point can be related to the bulk velocity. However no consistent outflow profile could be retrieved from the results and thus the relation to the bulk velocity and thus mass flow is deemed questionable.

Therefore this project used a different approach in which the velocity, pressure and temperature are measured further in front of the EDF at position V1. Position V1 has been chosen since it is right behind the honeycombs where the flow is expected to be most stable, but before the contraction so that the small disruptions caused by the probe are suppressed. There is also enough space for the temperature and static pressure probe.

Initially a direct relation between the velocity at V1 and V3 was established. V3 is right in front of the intake and rotor blades at the rotor mean radius r_m. After the relation is established the probe at position V3 is removed to allow for non-disruptive inflow of the air. In this approach the velocity is determined so close to the rotor that there is no space for the temperature and static pressure probe. This relation is shown in figure 4.3.

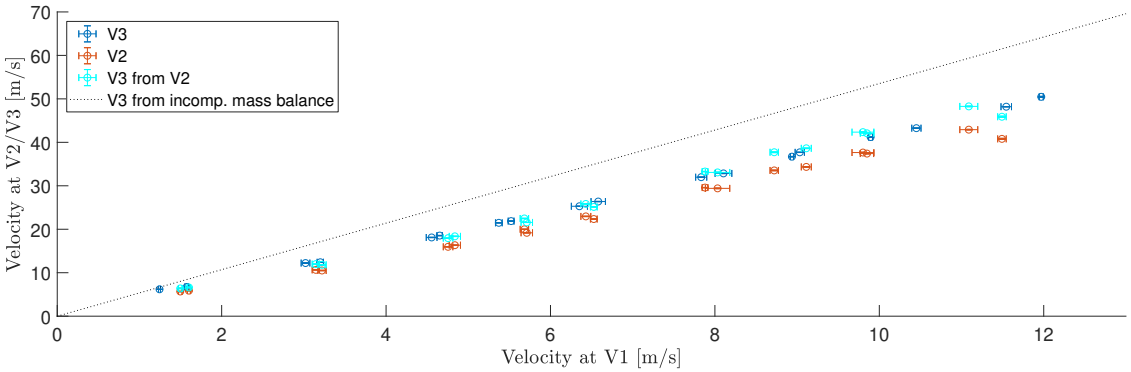

Figure 4.3: Relation between the velocity measured at V1 and V2/V3. Using the relation between the surfaces A2 and A3 one can achieve V1 vs V3 from V1 vs V2. The dotted line is V1 vs V3 according to in-compressible mass balance.

The relation between V1 and V3 does however not comply with the expected relation that results from equation 4.2. Explanations for this can be a non-uniform flow at either of the positions and/or changes is fluid density. Therefore a relation was also established between V1 and V2. V2 was chosen because measurements performed by R. Coolen showed that at this position the flow is

relatively uniform. The most severe deviations from the mean velocity at V2 are 5%. Additionally V2 allows for the installation of the temperature and pressure probe.

No difference in temperature was measured between V1 and V2, and the maximum difference in static pressure is only 1000 Pa, see appendix G The maximum variation in density is therefore less than 1%. Moreover the relation between V1 and V2 has the same deviation from the theory as the relation between V1 and V3. Calculating V3 from V2 using the ratio of the surfaces A2/A3 even gives a nearly identical relation as the direct relation between V1 and V3.

Measurement results of the velocity as function of the radius at V1, performed by R. Coolen show that the flow profile at V1 is not uniform, see appendix G. Using these measurements an estimation can be made of the bulk velocity at V1. Since the measurements of R. Coolen are performed in different conditions this correction is not completely accurate, but as can be seen in appendix G, the corrected points lie significantly closer to the theory.

It can thus be concluded that the mismatch between the theoretical and the measured relation between V1 and V3 is caused by a non-uniform flow profile at V1. The relation between V1 and V2/V3 is however very consistent as long as the velocity sensor at V1 is not moved. The data of V1 can thus be used to estimate the velocity at V3, and the mass flow rate through the accelerator. When the sensor is moved or a change is made to the setup, a new calibration is required.

Chapter 5

Vibration and deformation measurements

Camera measurements where performed in an attempt to link the unexpected decrease in thrust at increasing values of J to possible blade deformations and vibrations. The behaviour of the 3D printed material had not yet been investigated under load and the relatively low stiffness was a point of concern. The first series of measurements focused on capturing blade deformations, especially around the on-design point of J=1.03. The second series focused on blade vibrations. For each series different camera setups and settings where used. These, and how the images are further processed will be described in the next sections.

5.1 Deformation measurements

Deformation of the blades was not only appointed as a probable cause for the lower value of C_F at the on-design point J=1.03. But also for lower values of C_F for advance ratios above J=0.9 in general. For higher values of J the rotational speed decreases with respect to the axial velocity (by definition). Thus, centrifugal forces acting in the radial direction of the blades decrease with respect to the axial forces resulting in the blades being more prone to bending.

The inspection for deformation is done by converting images of the tip of a rotor blade to contours that can be placed over each other. This is done for different conditions. The process is described hereafter starting with the choice of equipment and settings. Thereafter the post-processing of the taken images to contours is described.

The measurements were done using the JAI GO 5000-M USB camera of which the properties are described in section 4.1.3. This camera was chosen since it was readily available and easy to install due to its size. A 35-mm 1.4-f lens was used at a distance of 30 cm from the tip of the rotor blades. This allowed the camera to be focused on the tip of the rotor blades while the marker placed on the hub was still identifiable. See figure 5.1 for a visual impression. The black dash is the marker that is placed on the hub. With this marker the rotational position of the rotor at each image can be compared. This lens and distance choice result in a resolution of approximately 0.05 mm per pixel at the distance of the focused object, which was assumed sufficient. The ROI could be reduced to 460x432 pixels (WxH) allowing for framerates up to 280 fps. Available as well was an extra light source which allowed the shutter time to be set to the minimal 10 ns without any difficulties.

Figure 5.1 shows an example of a frame shot by the camera. In operation air would flow from the left to the right side of the image. The tip of the rotor blade has been marked black in order to

increase the contrast. Below the rotor blade the black marker that is placed on the hub is visible. The edge on the right side of the image is the housing.

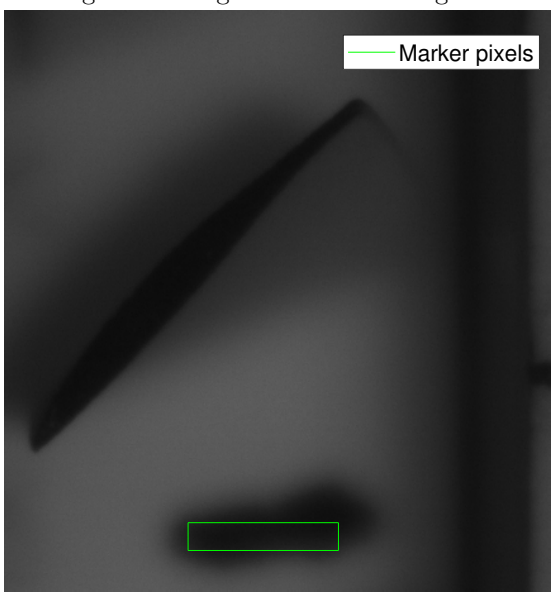

Figure 5.1: Image as shot by the camera. In this case the reference image where the rotor is stationary and the air velocity is 0. The pixels used for image identification are marked by green lines

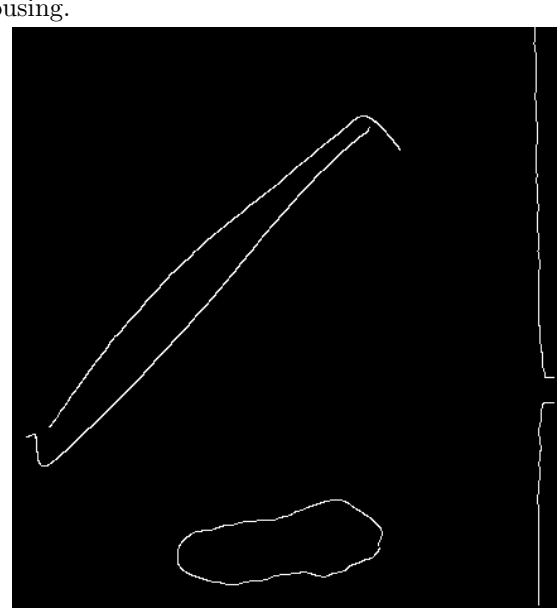

Figure 5.2: Canny filtered projection of the reference image shown on the left

The first step is to verify that the rotor is in the same rotational position as the reference frame. For this the marker on the hub is used. Using a reference image taken in stationary conditions, the pixels that cover the marker are selected. In figure 5.1 these pixels are marked by the green lines surrounding them. These pixels are than converted to a binary value, black(0) or white(1). When the total value of the selected pixels is smaller than the chosen threshold, the image is approved.

When the image is approved the next operation is the application of a edge detection filter. Most suitable for this turned out to be Canny filtering technique which is implemented in Image Processing Toolbox of Matlab. With the right threshold value, which was determined using trial and error, images as presented in figure 5.2 are achieved.

The last step is to convert the Canny filtered projection to a line format. These can be plotted and placed over each other more clearly. From these overlays the deformation magnitude can be determined as will be discussed in the next section.

5.2 Deformation measurement results

Initial testing was done with the rotor locked into position. Air was blown by at up to 45 m/s to check whether measurable deformation occurred. At the higher velocities of 27.0 ± 0.9 m/s and 45 ± 1.5 m/s deformation became detectable, see figure 5.3.

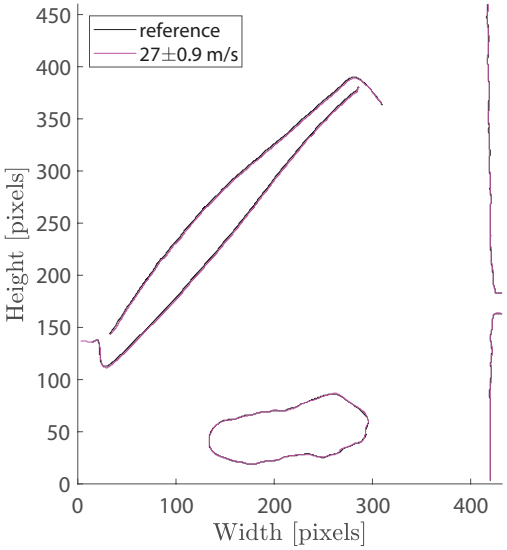

Figure 5.3: Blade outlining at $27.0 \pm 0.9 m/s$ compared to the outlining of the stationary reference image. Image from Run 31 (rotor 1)

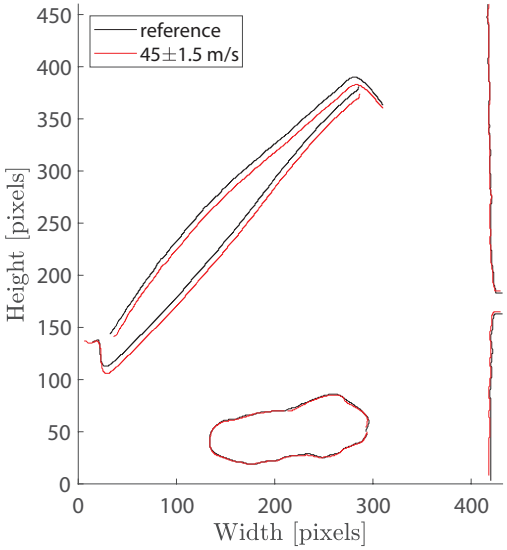

Figure 5.4: Balde outlining at $45 \pm 1.5 m/s$ compared to the outlining of the stationary reference image. Image from Run 31 (rotor 1)

At 27 m/s the first detectable deformation of the blade tip occurs as can be seen in figure 5.3. At this velocity the deformation is 0.12 ± 0.05 mm and the net force on the EDF is -5.0 ± 0.2 N. At 45 m/s the net force decreases to -11.4 ± 0.3 N and the deformation of the blade tip increases to 0.35 ± 0.05 mm. For both cases the deformation seems to be uniform and thus does not rotate the blade. It can be concluded that deformation does take place and increase with increasing force. Table 5.1 and 5.2 show the net forces measured on the EDF for comparable intake velocities at different operating conditions.

C_{a0} [m/s]	35.6±0.2	35.6±0.1	35.7±0.2	35.4±0.2	34.7±0.2	35.4±0.5	34.8±0.2
J [-]	0.62*	0.72*	0.89*	1.03±0.01	1.17±0.01	1.48±0.02	1.77±0.01
F_T [N]	12.1±0.3	9.3±0.3	4.5±0.3	1.9±0.2	-0.1±0.2	-2.1±0.2	-3.4±0.2

Table 5.1: Net force measured by the load cell for Run 75. *uncertainty smaller than projected decimals

C_{a0} [m/s]	48.0±0.6	45.6±0.3	44.4±0.3	44.5±0.2	44.6±0.2
J [-]	0.62±0.01	0.78*	0.99±0.01	1.34±0.01	1.81±0.01
F_T [N]	20.9±0.4	12.6±0.3	4.7±0.3	-1.5±0.2	-4.9±0.2

Table 5.2: Net force measured by the load cell for Run 74. *uncertainty smaller than projected decimals

These results show that the net forces in the higher advance ratio region ($\approx> 1$) are not larger than 5 N at even the highest measurement speeds. The deformation is therefore most likely limited to 0.12 ± 0.05 mm around the on-design point.

It is expected that this scale of deformation does not influence performance. This, since the net force, end thus deformation increase for for increasing 'flight' velocities. If deformation would influence performance this would mean that the performance of the EDF changes when it is operated at higher velocities, and thus higher net forces. However this behaviour is not observed within the uncertainty range of the performance measurements. At all of the test velocities the

behaviour of C_F seems equal. It is therefore concluded that the influence of the deformation of the blade does not have a detectable influence on the performance, at least up to the speeds achieved in the test setup. At higher velocities the effect can increase.

In theory it would also have been possible to execute the deformation measurements with a rotating rotor. This however seemed more difficult then expected. Considering the results and conclusions of the static rotor tests, the tests with a rotating rotor have not been executed.

5.3 Vibration measurements

As with deformation, blade vibrations may also be the cause of a decrease in performance. Although it was not possible with the current equipment to measure blade vibrations while rotating the rotor insight was gained on how the blades respond to air in an over-pitched position.

Initially the images shot with the 5000-M GO where used where the rotor was in a locked position. This to check if any vibrations measurable by camera occurred at all. A frequency that was expected likely to occur was the resonance frequency of the blade. An estimation of the first resonance frequency of the blades was done by assuming the blades to be fixed cantilever beams. For fixed cantilever beams equation 5.1 can be used to determine the first resonance frequency [20].

$$f_1 = 1.875^2 \sqrt{\frac{EI}{mL^4}} \tag{5.1}$$

With E the tensile modulus of the material, L the length of the beam, m the mass per unit length and I the second moment of inertia of the cross section. The tensile modulus of the material is 1700 MPa and the length of the beam is the length of the blade which is 62 mm. The mass per unit length equals the density of the material, 960 kg/m^3, multiplied with the surface of the cross section. Using Siemens NX the cross sectional area is determined to be 23.1 mm^2 which gives a mass per unit length m of 0.0222 kg/m. The second moment of inertia is determined with Siemens NX as well and is 4.796 mm^4.

Filling in these values result in an natural frequency of around 606 Hz. It has to be noted that this is just an approximation since the blades are twisted and thus not a simple cantilever beam. Also the cross surface of the blade is not constant over the blade height. Still, it can be expected that the natural frequency is way higher than the frame rate of the 5000-M GO.

However if oscillations at the first eigenmode occur it might be that they appear as an aliasing frequency in the data. Equation 5.2 can be used to relate actual occurring frequencies to aliasing frequencies [**?**].

$$AF = |CIMSF - IF| \tag{5.2}$$

In which AF is the aliasing frequency, CIMSF the closest integer multiple of the sampling frequency and IF the input frequency. For a sampling frequency of 280 Hz this gives that a frequency of 606 Hz would appear as $AF = |560 - 606| = 46Hz$.

To find possible blade vibration frequencies the following post-processing is done with the images. For a series of images the same procedure is followed as in section 5.1 to achieve Canny filtered images as shown in figure 5.2. Consequently the locations of the white pixels representing the blade edge are tracked in x direction for every row and in y direction for every column in each frame. This gives multiple signals: 1 for each row and 1 for each column in which a white pixel representing the blade is detected.

These signals are than averaged to gain 1 signal for the average location of the pixels in horizontal (x) direction, and 1 signal for the average location of the pixels in vertical (y) direction. Applying a discrete Fourier transform using the Fast Fourier Transform algorithm of Matlab a frequency spectrum of the blade (tip) vibrations can be created.

5.4 Vibration measurement results

Initial measurements with the 5000-M Go camera showed an increased activity around 100 Hz. Since the sampling frequency is only 280 Hz/fps there is a good possibility that the response visible at 100Hz is caused by aliasing. It was however shown that the used method works, it only needed more refining by using a higher fps. Therefore a second camera was installed, the PCO 1200hs. With the ROI set to 1280x200 (WxH) pixels it was able to shoot at a maximum of 2000 fps. Also a higher resolution was desired. Therefore a Navitar Zoom 1-6000 lens was installed which increased the resolution to 0.015 mm per pixel. With the available lighting the exposure time was set to 500 ns minimum.

The spectrum found by different velocities using the PCO camera is shown in figure 5.5, 5.6 and 5.7. Only the spectra for horizontal vibrations are shown. Because the response of the vertical vibrations and horizontal vibrations are nearly identical.

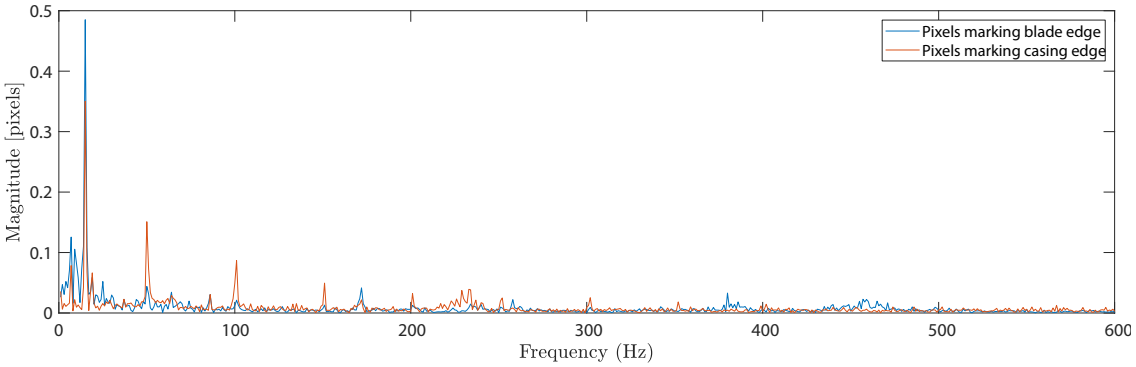

Figure 5.5: Single-Sided Amplitude Spectrum of horizontal vibrations at 4 ± 0.2 m/s. Resolution is 0.015 mm per pixel. Data from run 48 (rotor 1)

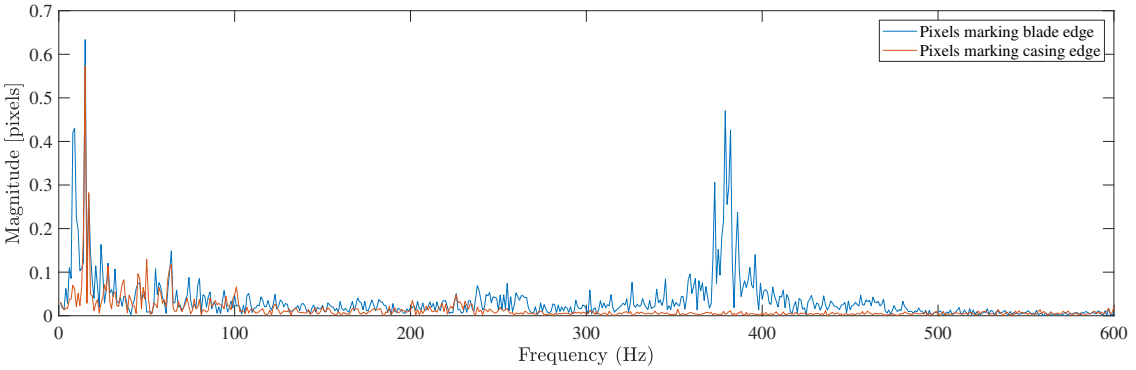

Figure 5.6: Single-Sided Amplitude Spectrum of horizontal vibrations at 19 ± 0.6 m/s. Resolution is 0.015 mm per pixel. Data from run 48 (rotor 1)

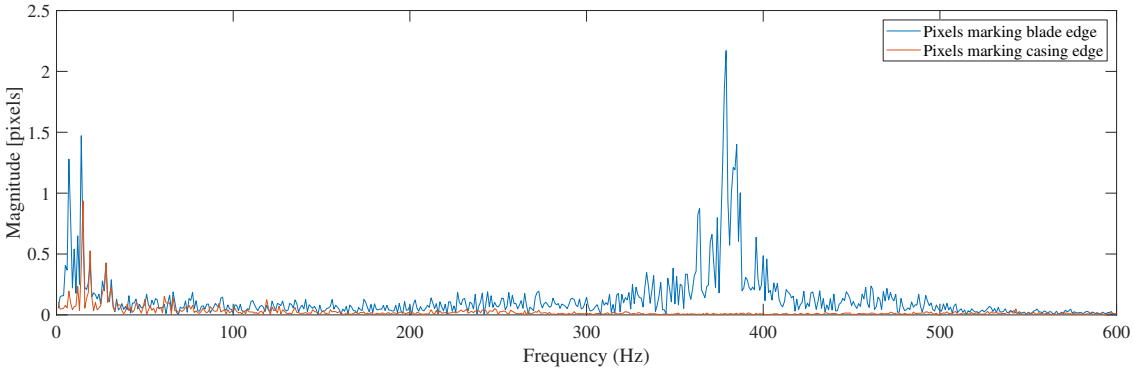

Figure 5.7: Single-Sided Amplitude Spectrum of horizontal vibrations at 36 ± 0.8 m/s. Resolution is 0.015 mm per pixel. Data from run 48 (rotor 1)

Vibrations of the blade were found around 380 Hz that intensify with increasing air velocities. To identify whether these responses are oscillations of the blade and not oscillations of the camera itself relative to the EDF, the same procedure is executed for the pixels marking the edges of the casing. As can be seen these pixels do return increased activity around 380 Hz. That the frequency occurs at a constant frequency insinuates that this is the eigen frequency of the blade. No frequency is found around 100 Hz and using equation 5.2 it can be concluded that the 100 Hz peak is an aliasing frequency of the 380 Hz peak since 380-280=100 Hz.

A note that has to be put with these results is that the measurements have been executed with a maximum frame rate of 2000 fps. It therefore might be an aliasing frequency as well. However since the theoretical natural frequency is expected to be in the range of 380 Hz it is concluded that the found frequency is indeed the natural frequency.

Further research to confirm this could have been conducted. But as with the deformation measurements there does not seem to be a noticeable influence of the vibrations on the performance. The amplitude increases with increasing velocity. This however does not seem to oppose any detectable decrease in C_F for the higher velocities.

Chapter 6

Performance comparison of the rotor designs

The rotor designs from chapter 3 were produced and tested for dynamic performance. This chapter will discuss the results of the dynamic performance measurements and discuss the comparison of these results with the predictions made by the theory.

6.1 Dynamic measurement procedure

In order to get the dynamic test results the following procedure is executed. With the EDF in place the data acquisition from the DAQ and the multi-meter is started simultaneously, this to allow the timestamps from the DAQ signal to be used to cut the 9596p Multi-Meter signal, see 4.2.1. The EDF is stationary and no air is supplied via the accelerator so the first samples can be used to determine the offset voltage of the load cell. This, since this tends to vary every time the EDF is (re)moved, see section 4.2.1. Thereafter the air supply valve is opened until the desired velocity for the measurement set is (approximately) reached. Immediately after the flow is constant the EDF is started and set to the desired RPM. This RPM is held for a certain period of time before continuing to the next RPM and the procedure is repeated. The duration of the intervals depend on the measurement conditions. For the lower velocities intervals of approximately 20 seconds are used to allow for the logging of at least 15 data points by the multi-meter and approximately 5 manual entries from the tachometer. Velocities around and above 40 m/s cannot be sustained longer than 2-3 minutes by the air supply and the interval period is shortened to around 10 seconds. The measurements start at the highest RPM and descend during a measurement set. This is done because the voltage of the batteries drops over the duration of operation and this limits the maximum RPM available for measurements. The RPM's at which the EDF is operated depend on the chosen accelerator velocity and desired advance ratios.

In order to get a clear view on the performance, measurement points were desired with intervals of 0.05 for the advance ratios in between J=0.6 and J=1.2. This, as it is the region where the EDF should be able to deliver positive thrust. Also some extra points outside this spectrum are desired to spot possible trends.

Table 6.1 shows the desired operating rotational speeds for 20 m/s and 30 m/s. At these speeds it was expected that quite stable operation was possible. The measurements around and above 40 m/s cannot be executed regularly and on many points and are therefore to check whether the scaling of the results still holds for slightly higher speeds.

J [-]	0.3	0.6	0.65	0.7	0.75	0.8	0.85	0.9	1	1.1	1.15	1.2	1.4
AoA_m[°]	37	22	20	18	16	14	13	11	8.3	5.6	4.3	3.1	-1.2
20 m/s [kRPM]	13.8	x	6.3	x	5.5	x	4.8	x	4	x	3.6	x	3
30 m/s [kRPM]	x	10	x	9	x	8	x	7	6	5.5	x	5.2	4.4

Table 6.1: Selected RPMs for desired measurement points (approximate). Points at J=0.95 and J=1.05 are not present because for both velocities a measurement at the same value of J=1 was desired

Eventually the desired distribution of measurement points was not achieved in many of the measurement sets. This due to a variety of reasons. Firstly because controlling the RPM of the EDF did not go as smooth as expected. The RPM is controlled by turning a small knob manually on the servo controller which makes small adjustments difficult. Consequently feedback of the actual rotational speed has to be retrieved from the tachometer. This fine tuning takes quite some time with the added problem that the change occurs in steps, which are sometimes a couple hundred of RPM. Besides the RPM also the velocity of the accelerator can only be set quite roughly and varies up to a couple of m/s. Finally there are also the occasional human errors in setting the RPM. All together the measurement procedure is quite rough. But from the gathered data the actual conditions can be gathered quite accurately, be it that the measurement points distribution is not as desired.

Table 6.2 shows the measured values found using the measurement procedure for a common measurement. In this case run 41.

Step	1	2	3	4	5
F [N]	20.9 ± 0.4	12.6 ± 0.3	4.7±0.3	-1.5±0.2	-4.9±0.2
I [A]	69.0 ± 1.6	35.6 ± 1.0	16.9 ± 0.4	5.6 ± 0.3	0.8 ± 0.1
U [V]	22.82 ± 0.03	23.51 ± 0.03	23.99 ± 0.02	24.42 ± 0.01	24.71 ± 0.01
RPM	15997 ± 2	12072 ± 6	9324 ± 4	6874 ± 9	5119 ± 26
v_{V1} [m/s]	11.38 ± 0.15	10.81 ± 0.07	10.51 ± 0.07	10.54 ± 0.05	10.56 ± 0.05
$p_{V1} - p_a$ [Pa]	-128.4 ± 7.5	381.0 ± 4.4	798.3 ± 1.5	1209.2 ± 0.8	1443.6 ± 3.6
T_{V1}	21.7 ± 0.14	21.1 ± 0.07	20.8 ± 0.00	20.8 ± 0.00	20.8 ± 0.05

Table 6.2: Measured quantities from Run 41 (target 40 m/s). The uncertainties are that of a single standard deviation multiplied with the student-t value corresponding with the amount of samples. *The offset values measured in the stationary positions. Values shown in the table are corrected for these offsets.

The values and uncertainties for the force, current and voltage are acquired by calculating the mean and standard deviations of the samples that are selected from the measurement. Except for the RPM, all these samples are cut out of the signals that span the entire measurement duration. This procedure is discussed in section 4.2.1, and examples of this for the force and current sample are shown in figures 4.2a and 4.2b. Finally, to achieve the values for the dimensionless parameters J, C_F and η_{system} that will be used in this section, the parameter values from table 6.2 values are entered in the corresponding equations for these parameters as described in section 2.4. Using the error propagation method as described in appendix E the uncertainties presented in table 6.2 are accounted for.

6.2 Comparison with old measurements

Most significant are the thrust characteristics. As described in section 2.7 a convenient way to present the thrust results is by the thrust coefficient C_F and the advance ratio J. Figure 6.1 shows

the old results for the dimensionless thrust coefficient compared to the new results.

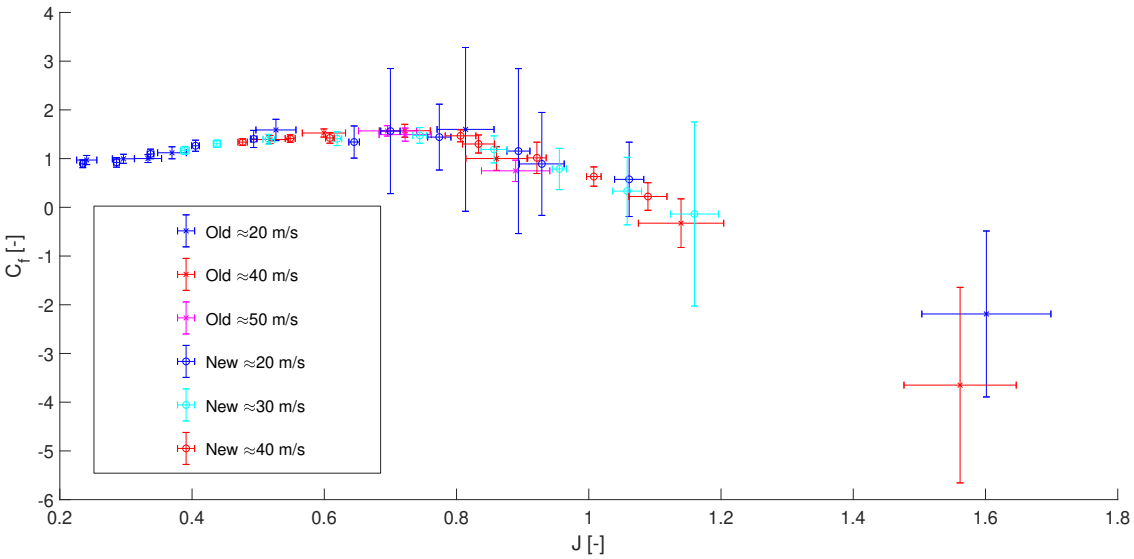

Figure 6.1: The measured thrust coefficient versus the advance ratio for rotor 1. Data for rotor 1 is from run 0.5, 0.6, 0.7, 40, 41 and 42)

As can be seen the results of the new measurements seem to align with the results of the old measurements within the uncertainty range of the measurements. The uncertainties in the coefficients are presented by the error bars. These are calculated with the error propagation method described in Appendix E using a single Sample Standard Deviation (65%) of the involved quantities. No new measurements have been done at approximately 50 m/s because the new accelerator cannot provide a stable flow of air long enough at this velocity.

As mentioned, the new results fit within the uncertainty range of the old results for inside as well as outside the efficient operating range. What happens outside the operating range is less relevant for this project and is not studied closely. Nevertheless, a short explanation of the general behaviour of the EDF will be given, which is valid for all the tested rotor designs. For lower advance ratios engine stall occurs. Initiating around J=0.6/AoA=22.3° for the reference rotor, one can see that the thrust coefficient starts to decline. No complete stall seems to occur however, and the thrust coefficient seems to level out. A cause of this behaviour is probably the closed environment created by the accelerator. The only air flowing through the EDF is the air supplied by the accelerator. In actual flight an aircraft engine will suck in additional air, or deflect air depending on the operating conditions. The accelerator will only supply a certain amount of air, or force a certain mass flow through the EDF. So although the EDF is most likely to stall in in-flight conditions, the accelerator keeps forcing air through, preventing complete stall and a severe drop in the thrust coefficient.

On the other side of the spectrum were the advance ratio increases the thrust coefficient drops as well. This due to the fact that at a certain point the blade is 'under' pitched and the angle of attack of the blades becomes to small to generate lift. The accelerator keeps forcing air through the EDF inducing drag and thus creating negative thrust.

The rest of the presented results will be in the range of J=0.4 up to J=1.3 and not the entire range of J that can be covered with the setup. This, because the performance range of all the rotor designs fit well within these bounds allowing results within the operating range to be inspected more closely.

The measurements inside the operating range overlap within the given uncertainties. Which, seen the uncertainties of many measurement points, is not very conclusive. A Discrete Four-

ier transformation with the Fast Fourier Transform algorithm of Matlab is performed on these measurements to allow for a spectral analysis.

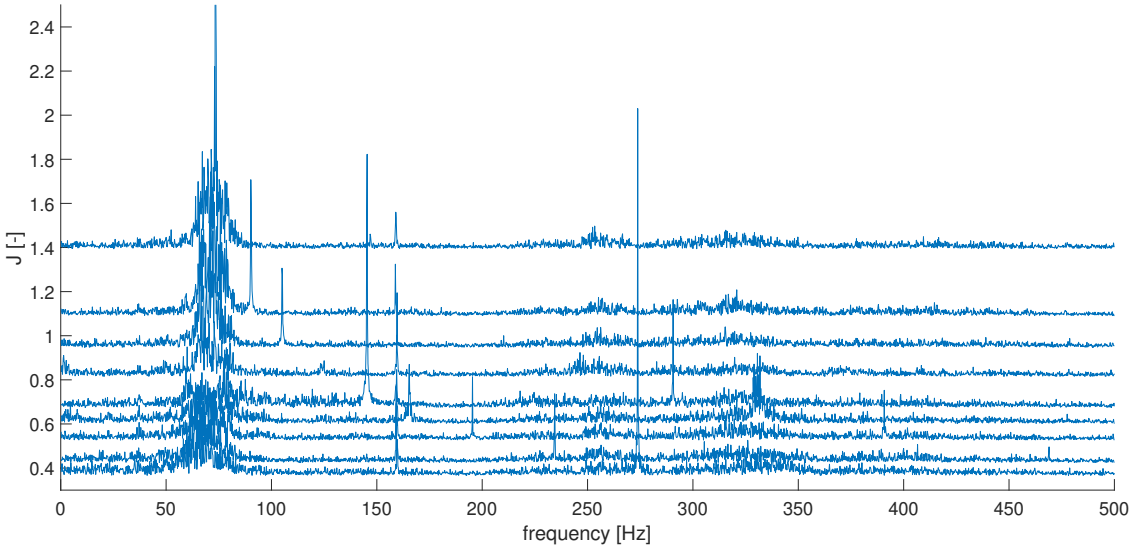

Figure 6.2: Single-Sided Amplitude Spectra of force sensor signal of Run 41. (Rotor 1 at approximately 30 m/s)

In figure 6.2 sharp peaks are visible that increase with decreasing advance ratio. These peaks are located at the frequencies that exactly match the RPM's and are caused by an unbalance of the rotor. Furthermore a sharp constant peak around 159 Hz can be observed. A peak around this frequency is also observed in older measurements and in static measurements in which the setup was different. The peak therefore seems to be related to the EDF itself or the electric circuit, since nothing was changed to these components with respect to the older measurements. Mechanical vibrations seem unlikely due to the high frequency, but the exact cause is however still unclear.

Secondly, noise is found from roughly 50-100 Hz and in weaker form between 250-350 Hz. The noise consistently appears in all of the measurements. The noise seems to be to high for mechanical vibrations. However nothing similar or a relation to this noise is found in the current and voltage data. Where it originates from is thus unclear.

To remove the noise a low-pass filter is applied to the loadcell data. Figure 6.3 shows the comparison of the old and new data points with the filtered loadcell data.

The dimensionless thrust of the old and the new measurement series do not seem to overlap completely. The cause of this could be one of the following: The measured RPM, Force, velocity or estimation of density in one, or both of the series are not measured correctly. Due to the low velocities density effects before the intake can assumed to be negligible. Also the RPM is unlikely to be the cause since the tachograph is accurate and used the same way in all sets. This also holds for the loadcell measurements. The same equipment is used and a calibration done in this research delivered nearly identical results to that of the previous research. A wrongly entered offset could be the cause, but since the peak of C_F in both measurements has a similar value, this is unlikely.

Since the measurement technique, as well as the accelerator have been changed in between the measurement sets it is very likely that the cause lies within the estimated intake velocity. In the case that the intake velocity is estimated incorrect a shift of the curve in x direction appears. Since there is a linear relation between C_{a1} and J this shift becomes more severe as J increases.If This is exactly what seems to occur. Which of the measurements is closest to the real value cannot be said with complete certainty. However the new method does use more accurate equipment

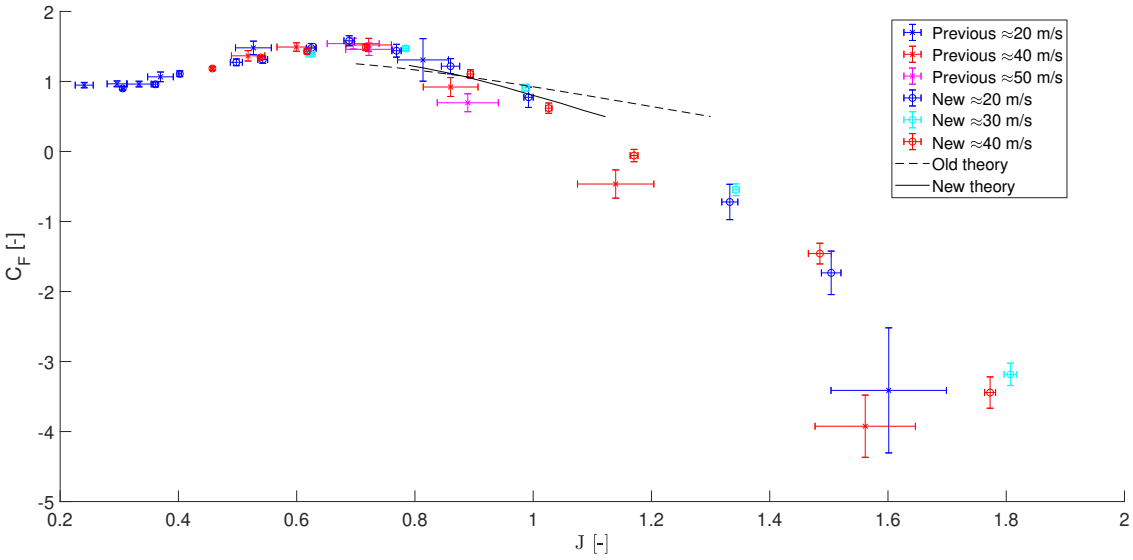

Figure 6.3: The old and new predicted and the measured thrust coefficient versus the advance ratio for rotor 1. Data for rotor 1 is from run 0.5, 0.6, 0.7, 40, 41 and 42

and bases the estimation on a more stable point in the flow, see section 4.3. Therefore the new measurements result will be used for further analysis.

The new theoretical prediction approaches the results of the measurements more closely than the older model. This can be quantified using the coeficient of determinations which is 0.82 for the new model versus a value of 0.57 for the old model. Still it grossly underestimates the thrust coefficient around J=0.8. Even when an isentropic efficiency of 100% is assumed, the model does not predict the peak values of C_F to be as high as is measured. An explanation can be the fact that the theoretical prediction is purely based on the performance of the EDF at mid-span design and under conditions for vortex free flow. When operated off-performance these condition are not met, see section 2.10. This could lead to a different distribution of the mass flow as follows.

In case of vortex free flow the interaction between the rotor and stator vanes is such, that the elements of the fluid are in radial equilibrium and the mass flow is constant over the annulus, see [6]. When the conditions for vortex free flow are not met a different distribution of the mass flow will be present. This makes a prediction based on the mean radius parameters less accurate. How the mass flow will be distributed at a certain performance is difficult to predict and can be approximated using streamline curvature theory. This is however outside the scope of this project.

On the higher advance ratio end the model seems to over estimate the thrust coefficient slightly. This could partially be due to the effect described above. A second possible factor is that the drag coefficients used in the efficiency calculations are under-estimated. This can be due to a variety of reasons ranging from the roughness of the blades and an unbalance of the rotor to a high amount of tip leakage.

6.3 Power consumption

The power consumption of the system is presented in the system efficiency as defined by 6.1. Although knowledge about the power consumption of the rotor is preferred, no accurate estimation can be made with the current setup, see section 2.4. Figure 6.4 shows the system efficiency versus the advance ratio of the old and the new measurements.

$$\eta_{system} = \frac{FC_{a1}}{I_{in}U_{in}} \tag{6.1}$$

With I_{in}, U_{in} and F as measured and C_{a1} as approximated with the velocity relation. See figure 6.4

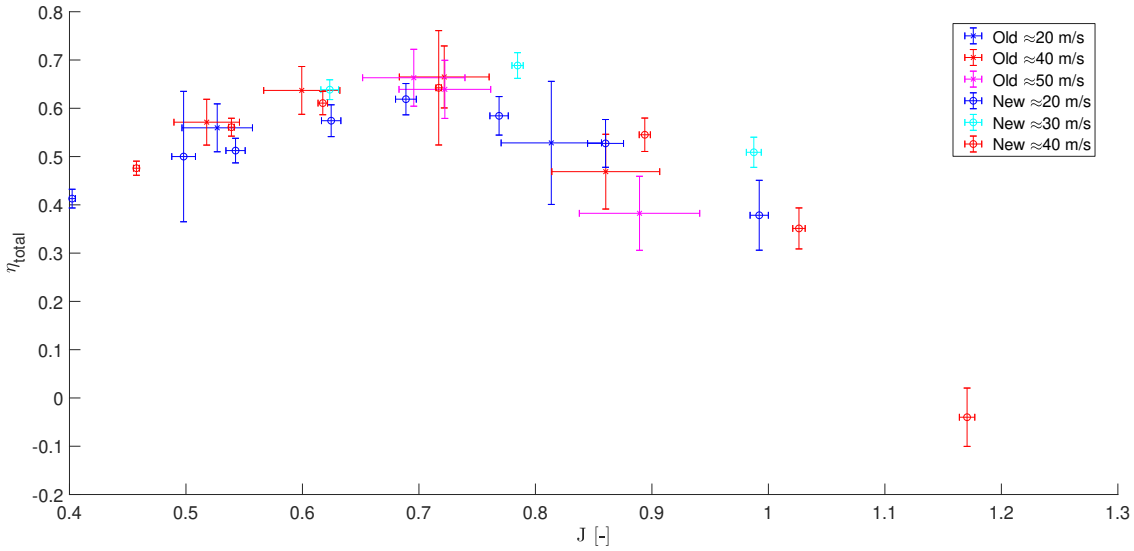

Figure 6.4: Total efficiency of the system versus the advance ratio

The results look very similar to the results in figure 6.3. This is no coincidence. Results in [15] show that power consumption roughly scales with the square of the rotational speed. C_F contains the square of rotational speed in the denominator and the thrust produced in the enumerator. One therefore finds a very similar relation between η_{system} and C_F as long as the drag forces do not become dominant.

The efficiency at 20 m/s seems to be lower than for the higher velocities, especially in the new measurement sets. This behaviour is found for all the newly tested rotors. This seems counter intuitive but is most probably caused by the low efficiency of the electric engine when operated in low power settings, see appendix F. The data for the lower velocities is therefore not used in comparing power consumption.

As in figure 6.3 a difference is present between the new measurements and the old measurements. This can be explained to have the same cause. Which is a shift of the data in J due to incorrect measurements of the intake velocity.

The system seems to achieve a top efficiency around 65%. With a gross estimation of an ESC efficiency of 85% and an engine efficiency of 92 % -which were adopted from [15]- the EDF efficiency is 83%. The operating point for this efficiency lies around J=0.75 which is at a slightly higher advance ratio than the operation point at which C_F is at its maximum.

Since the information resulting from the efficiency curves is very similar to that of C_F, comparison of the rotor designs is discussed on the base of the thrust coefficient curve.

6.4 Test results rotor 2 and 3

Figure 6.5 shows the thrust coefficient of rotor 1, 2 and 3 vs the advance ratio as calculated from measurement data as well as from the model. For each rotor, the measurement sets of

approximately 20 m/s, 30 m/s and 40 m/s are combined. The theory only covers a limited operating range that depends on the design.

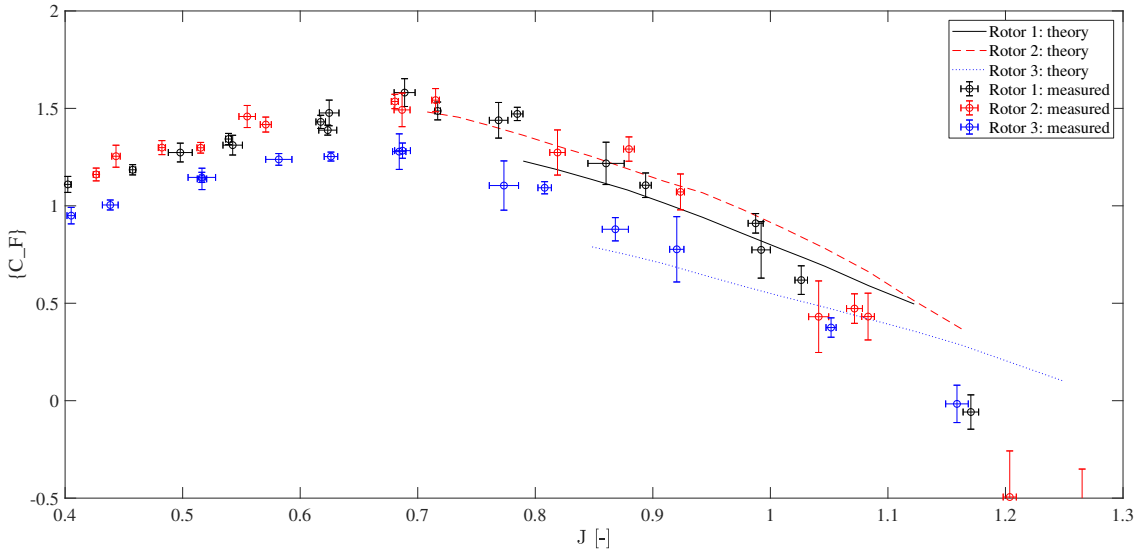

Figure 6.5: The predicted and the measured thrust coefficient versus the advance ratio for rotor 1, 2 and 3. Data for rotor 1 is from run 40, 41 and 42. Data for rotor 2 is from run 45. 46 and 47. Data for rotor 3 is from run 68, 69 and 70

The measurement results of the 19 bladed rotor and 13 bladed rotor seem to completely overlap. This is in contrast with the model that predicted a slightly higher thrust coefficient for the 19 bladed design, especially at lower values of J. Also, the model predicted a wider operational range for the 19 bladed rotor than the 13 bladed rotor which does not seem to hold.

Interestingly enough the power consumption and thus efficiency also seems to be very similar to the 13 bladed rotor. This induces the suggestion that as well total lift as total drag forces are similar in both designs. The cause of this could be that the mass flow is distributed more to the outer radius of the annulus. This increases the velocity in the outer region of the annulus which decreases the angle of attack. Added that the camber and solidity are also lower this can result in less deflection and also less drag. This would mean that at the inner side of the annulus mass flow decreases, with which axial velocity decreases. This increases the angle of attack in this region. However due to the design angles of attack in these sections are already relatively large and thus a further increase only causes stall to emerge earlier, which in turn shortens the efficient operating range.

Also possible is that for some reason the ESC or engine operated at a higher efficiency, compensating the efficiency drop of the rotor. This could be caused by extra losses due to increased secondary flows or increased tip leakage. It has to be noted that the amount of data points of the 19 bladed rotor from which this conclusion is drawn is very limited. This, since the points at lower velocities (20 m/s) are not taken into account, see section 6.3. It thus cannot be said for sure why the 19 blade rotor seems to behave similar to the reference rotor, although it can be said that no real advantage arises.

The prediction of the behaviour of the 7 bladed rotor is somewhat more accurate in the fact that it expected a lower value of C_F in general. Also near the design point C_F is as predicted. It was however expected that the efficient performance range shifted slightly more to the higher advance ratio region. Put differently, the rotor was expected to operate at slightly lower angles of attack. This does not seem to be the case. One could intuitively say, that since nothing was changed to the individual blades this not surprising. However, measurements done by [11] which are concluded

in the carpet plots show that lower solidity blade rows are operable at lower angles of attack but also stall at lower angles of attack. Still, this is not the case.

Furthermore the gradient of C_F for the measurement results is steeper than the gradient predicted by the model. This is also the case for the reference rotor, but the effect seems to be more severe for the 7 bladed rotor. Multiple explanations can be given for this observation. Firstly because of the faster then expected decrease in efficiency, due to an increase of drag forces with increasing advance ratio. Similar to the prediction, the measurements do not show a significant decrease in efficiency. With the assumption that no extreme variations occur in the efficiency of the components it is thus more likely that the stronger gradient is the result of a stronger variation in lift and thus deflection. A possible explanation for a stronger deflection, and the unexpected efficient operation for low values of J, is yet again a change in the mass flow distribution.

As the RPM increases the mass flow is this time deflected more towards the inner radius of the annulus. This increases the axial velocity at the inner radius and decreases velocity at the outer radius. This in turn decreases the angles of attack at the inner radius and slightly increases the angle of attack at the outer radius. This decrease in angle of attack at the inner radius delays the occurrence of stall. The outer radius off the blades on the other hand have a smaller angle of attack by design, see table 2.1. An increase in angle of attack is therefore possible without inducing stall earlier.

In order to verify whether this conclusion referring mass flow is true one of the following options is suggested. Firstly the theory can be adapted better for 3D flow. In between the used model which only considers mid-span design and sophisticated CFD lie certain so called through flow or streamline curvature methods. These were not investigated further in this project, but could offer more accuracy in the near future. Also a more closer look into vortex theory and forced vortex design might offer more insight. Based on this theory new rotors can be designed with the purpose of testing how different degrees of reaction influence performance. From these measurement results one then may find a correlation. For the rotors discussed in this chapter this is unfortunately not possible since the most inner blade sections of the 19 bladed design and the most outer sections of the 7 bladed design lie outside the range of the carpet plots.

To conclude none of the designs seem beneficial. The 19 bladed design does not seem to offer any significant improvements nor disadvantages. The 7 bladed design greatly reduces thrust without any significant advantage.

6.5 Test results of rotor 4

The coated rotor performed significantly worse than the reference rotor. It is likely that this is due to the application of the coating. This has been done manually and visual inspection of the rotor shows that the thickness of the coating varies. This changes the cascade shape as well as that it induces an imbalance of the rotor. It is expected that this causes the poor performance of this rotor. The measurement results are presented in appendix D.5.

6.6 Test results rotor 5

In figure 6.6 the measurement results of the fifth rotor design are compared to the reference rotor for all velocities. Also the theoretical predictions are added for comparison.

The model did not really predict any real difference in performance. A small improvement, although not predicted by the model, was expected due to the smoother upper and lower edges of the fifth rotor. This does not seem to be the case and the rotor appears to behave nearly identical to the reference rotor. The peak value of C_F seems to be slightly lower for rotor 5 although more

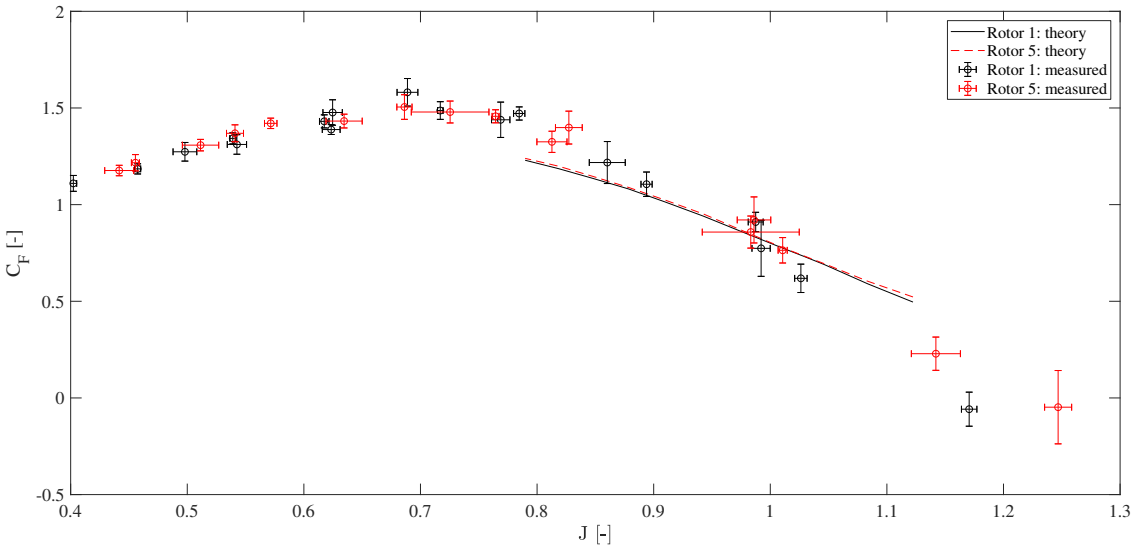

Figure 6.6: The predicted and the measured thrust coefficient versus the advance ratio for rotor 1 and rotor 5. Data for rotor 1 is from run 40, 41 and 42. Data for rotor 5 is from run 62, 63, 64

measurement sets are required to confirm this. If this appears to be the case the difference is however marginal.

It might appear from figure 6.6 that rotor 5 seems to achieve slightly higher values of C_F for higher advance ratios. Measurement results beyond the projected operating range show that this is not the case. Finally there does not seem to appear a detectable difference in system efficiency compared to the reference rotor.

It can be concluded that the procedure used in rotor 5 for adapting the cascades does not offer a significant advantage in comparison with the method used in rotor 1. A note has to be put that the blades of rotor 5 are slightly thicker, thus stiffer and most likely stronger than that of rotor 1. May a different material ever be used that demands stiffer blade design the method used in rotor 5 can be used to get similar results as for rotor 1.

6.7 Test results rotor 6

Lastly figure 6.7 shows the measurement results for the rotor with the adapted stagger angle of the blades.

The shift in the measurement results, at least for the predictable operating range, is as intended. A measurement point at $J = 1.02 \pm 0.01$ gives a value of $C_F = 1.01 \pm 0.07$. This is slightly higher than expected and is caused by the error of the model. The theory seems to wrongfully predict the measurement results in a similar fashion as the reference rotor. This is not a surprise since the shape of the blades is equal to that of the reference rotor.

There does seems to be a slight increase in the peak value of C_F for rotor 6. An explanation can be given using equation 2.14 and the carpet plot shown in figure 2.6. When the stagger angle of the blade is decreased the angle of attack increases with respect to the air inflow angle. In other words, rotor 6 has a higher angle of attack than rotor 1 for equal air inflow angles. From the carpet plot in figure 2.6 it can be deducted that for lower values of the air inflow angle, a cascade row can operate up to higher angles of attack, and thus generate a greater deflection. Comparison of rotor 1 and rotor 6 shows that rotor 1 reaches it peak value of C_F at an air inflow angle of

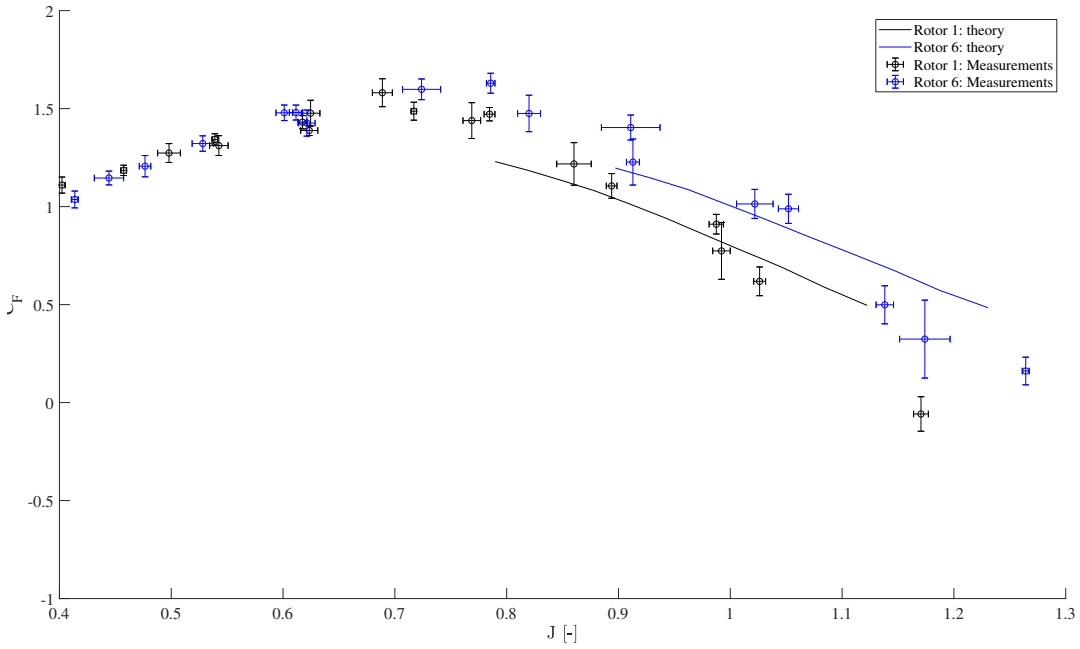

Figure 6.7: The predicted and the measured thrust coefficient versus the advance ratio for rotor 1 and rotor 6. Data for rotor 1 is from run 40, 41 and 42. Data for rotor 6 is from run 65, 66, 67

approximately 55 degrees, while for rotor 6 this occurs at an air inflow angle of around 50 degrees. This means rotor 1 can operate up to an AoA of roughly 21 degrees while rotor 6 can operate up to an AoA of roughly 23 degrees.

To conclude, rotor 6 has been designed such that it provides more thrust at the design point, with the expectation that higher flight velocities might be reached. Therefore a comparison of this rotor is done with the reference rotor using the theoretical drag model of the aircraft from [15]. From the model follows that, for a single EDF, the maximum speed is 146 m/s instead of 158 m/s. Instead of an increase the top speed thus slightly decreases. In the next section the cause for this will be discussed.

Chapter 7

Expected in flight performance of the EDF

Determining the thrust of the EDF for varying flight velocities does not purely depend on the performance of the EDF itself, but also the performance of the motor. This chapter will discuss how the two combined perform. The reference rotor is discussed as well as rotor 6, since it was expected to perform better at higher flight speeds.

7.1 Prediction of thrust for varying flight speeds

The maximum shaft power the electric motor can supply varies with rotational speed. For lower rotational speeds the maximum power declines, see figure F.2. This provides a bounded area in which the EDF can operate. On one hand the rotational speed should not increase to much to prevent stall. On the other side decreasing rotational velocity severely decreases the power available from the motor. If the drop in motor power outpaces the drop in required power by the rotor the available thrust plummets. See figure 7.1.

The curve showing the aircraft drag is the model from [15]. Although this prediction may be way off from what the actual drag will be it offers a good practice for implementing EDF design into an aircraft. The maximum thrust curve is based on fits through the data of C_F and η_{system} within the efficient operating range. The ESC efficiency is assumed constant at 85% and the motor efficiency at a constant 92%. With these efficiencies known the rotor efficiency can be deducted from the system efficiency. As mentioned in section 6.3 the assumption of constant ESC and motor efficiency could differ quite a lot from real conditions.

The maximum power curves go through different sections. The first 'hollow' part is where the EDF is operated at maximum RPM, or minimum J before stall occurs. Then the maximum RPM of the motor is reached and the advance ratio starts to increase with increasing inlet velocity. At this point both rotor designs reach their maximum thrust. Then a rapid decline sets in which is caused by the motor reaching its maximum power output. The advance ratio at which the motor can operate now, and thus the thrust than can be produced, depends on a combination of the power available by the motor and the efficiency.

For future design purposes it is important to understand how differences in the thrust coefficient curves translate to that of performance for varying flight speeds. The next paragraph describes the causes leading to the differences seen from rotor 6 with respect to rotor 1.

In the first stage less thrust is produced, since rotor 6 stalls earlier than rotor 1 and the maximum

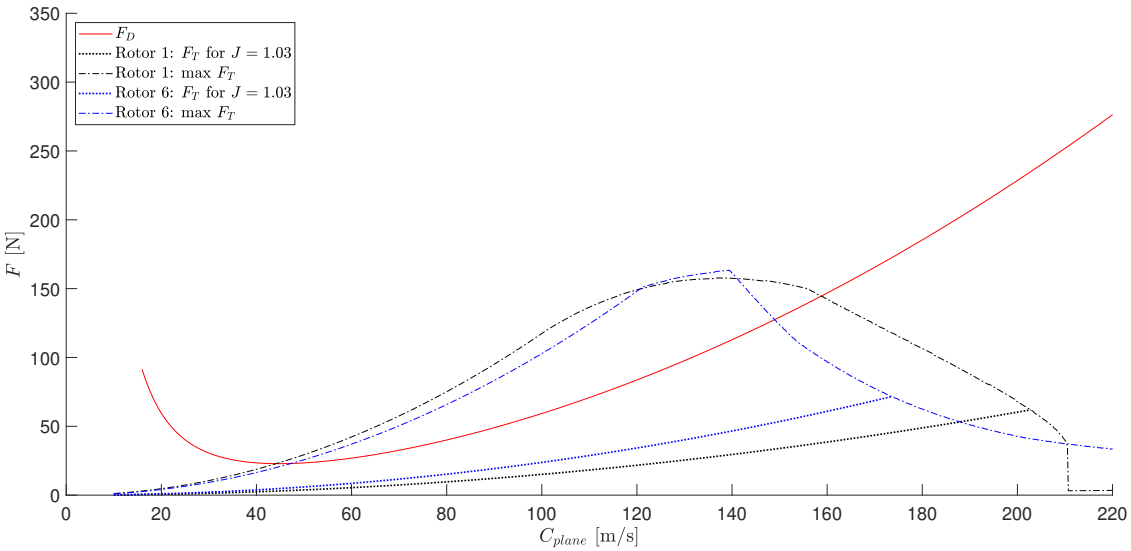

Figure 7.1: Aircraft drag (by the model of J. Oorschot) and thrust production of a single EDF with rotor 1 or rotor 6 for varying flight speeds.

RPM is thus lower. Later than for rotor 1, RPM becomes limiting. Also rotor 6 produces more thrust than rotor 1, which is as intended. However earlier than expected, the maximum power output of the motor is reached and the thrust produced drops even more rapidly than for rotor 1. This, because the rotor produces more thrust at higher values of J, which thus also requires a more severe drop in J to match the power output of the motor. Eventually however, where rotor 1 reaches negative thrust rotor 6 can still produce useful thrust.

From the constant advance ratio curves it can be deducted that rotor 6 does function as intended. However not enough power/torque is available from the motor for the optimal use of this design.

With the current assumptions for ESC and motor efficiency and the model for aircraft drag it can be concluded that for a single EDF motor none of the designs offer any improvement in flight velocity. At the peak velocity of 158 m/s the reference rotor operates at an advance ratio of 0.79. Approximately at this advance ratio the peak efficiency of the rotor is achieved which is around $65/(92 * 85) = 83\%$, see figureF.1. Since none of the designs peak higher than this value the reference rotor is for the current estimation the most optimal design. Of course improving efficiency can offer higher velocities, but only slightly. At 90% efficiency, which is very high for axial compressors, the maximum speed would only increase to 163 m/s.

Even with 2 EDF's it is most likely not possible to reach a speed of 208.3 m/s if the current model for drag is assumed. This would require an EDF efficiency of $(208.3 \cdot 247)/(2 \cdot 27781) \cdot 100 \approx 93\%$. Assuming that the maximum efficiency of the EDF is 83%, a velocity of 200 m/s can be achieved at which a drag force of 229N has to be overcome. This does require a redesign of the rotor. To extract the maximum amount of power from the motor, the rotational speed has to be 41991 RPM. Combining these numbers in the equation for the thrust coefficient one finds that a thrust coefficient of $C_F = 1.1$ is required at an advance ratio of J=0.99. Relative to rotor 1 this can be achieved as follows. The peak efficiency needs to shift from J=0.75 to J=0.99. This can be achieved by decreasing the stagger angle roughly 7 degrees. Also the camber needs to be decreased by a certain amount to allow for a value of $C_F \approx 1.1$ at J=0.99. The desired curve is shown in figure 7.2.

With the mentioned adaptions to the design it is thus possible to reach 200 m/s without any major improvements in C_F or the efficiency of the rotor. The only thing that has to be done is adapt the performance to as specified in figure 7.2. This does not seem to be a very big change considering

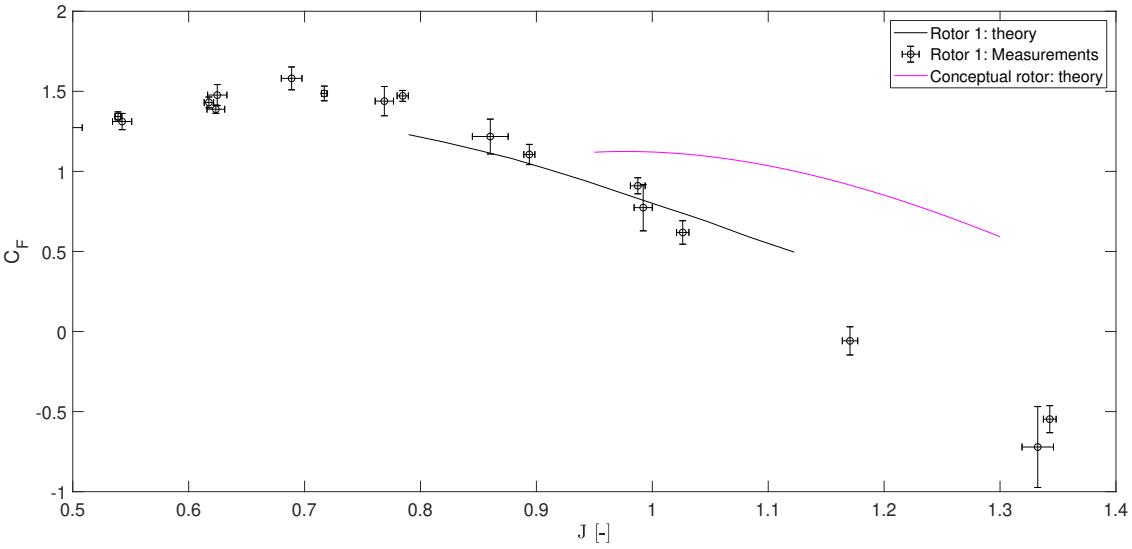

Figure 7.2: Coefficient of thrust for the reference rotor as expected and measured besides the thrust coefficient required for an increased top speed when 2 EDF's are used

the uncertainties and spread of the measurement points. The prediction is however very sensible to changes in C_F. If C_F is only 0.05 higher than required at J=0.99 the power consumption is to big and performance plummets before reaching 200 m/s. Besides it has to be considered that the test conditions in the setup are not entirely as in flight conditions, this will be discussed in the next section. Finally there are the assumptions for the efficiency of the ESC and the motor which are very rough. Together it can be said that the maximum speed reached with 2 EDF's will probably be higher when the conceptual rotors are used instead of the reference rotors. Although it will most likely not be 200 m/s.

Chapter 8

Conclusions

The purpose of this project was to get a better understanding of how rotor design influences the thrust production of the EDF over its operation range. The thrust and operating point have been found to be characterized well by the dimensionless thrust coefficient and advance ratio. The first target was to find the cause of the mismatch between the expected and measured coefficient of thrust over the efficient operating range of the reference design.

The cause of the mismatch in the measurement results and theoretical expectation in [15] was partly found to be caused by inaccurate estimation of the axial velocity at the intake. Therefore a different approach was taken in this research resulting in more accurate predictions of the intake velocity.

It was expected that the flexibility of the 3D printed material influences the performance, which causes the mismatch with the theoretical expectations. Therefore blade deformation and vibrations were measured using high speed cameras. It is concluded that the influence of deformation and vibrations on the measured results is most likely minimal. As speeds increase blade deformation and vibrations increase with it. For speeds that are significantly higher than the speeds achieved in the setup they might become non-negligible.

Aside from the measurements evaluation was done of the theoretical model used for designing the EDF and predicting its performance. It was found that some relatively simple improvements could be made. With these improvements the thrust characteristics predicted with the model corresponded better with the measurement results. Still, the prediction is not entirely within the uncertainty bounds of the measurements. And although being less severe than with the old model, the thrust coefficient is increasingly under estimated as the advance ratio decreases, and over estimated as it increases, see figure 6.3.

Non-uniform distribution of the mass flow can be appointed as a probable cause for this. The stage of the EDF has a hub tip ratio of 0.48 which is considered low. Still, a mean radius approximation can be representative for vortex free flow and uniform inflow conditions. Vortex free flow conditions can be met by designing the stage correctly. However, as the EDF is operated further from its design point these conditions are met to a lesser extend. This induces radial components in the flow that can not be neglected. The model does not account for this. Additionally non uniform intake conditions can be caused by the deflection of flow by the spinner. Besides the airflow provided by the flow accelerator is shown to deviate by 5% in [**?**]. In addition to the non-uniform mass flow theory there are losses that are not accounted for in the theory. Significant losses up to a couple percent can be caused by tip leakage and secondary flows. Also the nozzle and inlet induce variable losses reducing efficiency more than expected.

Based on the new model 5 additional rotor designs were created, produced and tested. These were compared to the theoretical predictions made by the model with the purpose of testing to what

extend desired thrust characteristics can be achieved. For all of the rotors it can be concluded that the new model does not predict the thrust characteristics of these rotors entirely correct over the wider operating range. However the predictions for the on-design thrust match reasonably well. Also the general difference with respect to the reference rotor can be predicted reasonably well.

One of the created rotor designs focused on achieving the on-design thrust as intended by j. van Oorschot in [15]. Which is a thrust coefficient of $C_F = 0.91$ at an advance ratio of 1.03. The new theoretical model was used to design this rotor. At an advance ratio of $J = 1.02 \pm 0.01$ this new rotor measured a thrust coefficient of $C_F = 1.01 \pm 0.07$. Compared to the reference rotor, which had a thrust coefficient of $C_F = 0.62 \pm 0.07$ at $J = 1.03 \pm 0.005$, this is a major improvement.

Eventually the overall target is to increase the maximum flight velocity of a future aircraft propelled by the EDF. In order to reach the highest speed available the engine should be operating at its maximum RPM at which it provides maximum power. Simultaneously the EDF should be operating at maximum efficiency at this RPM and flight speed. These conditions have to be matched with the overall drag characteristics of the plane.

Currently only the efficiency of the entire system can be determined. Therefore similar predictions as in research by [15] have been made about the efficiencies of several electric components. Also the prediction for aircraft drag has been adopted. With these assumptions it can be concluded that none of the new rotor designs achieve an increase in maximum flight velocity with respect to the reference design. For both a single as two EDFs the maximum estimated speeds of respectively 158 m/s and 185 m/s are achieved using the reference rotor.

A single EDF with the reference rotor equipped is expected to operate at the maximum RPM of the engine as well as at its peak efficiency. Higher flight velocities can therefore only be reached with more efficient rotor designs. With an estimated efficiency of 83% the space for improvement is however limited to only a couple metres per second.

Larger gains can be achieved in the situation that 2 EDF's are used. Different characteristics for C_F and the EDF efficiency are required. These have been determined but no rotor has been designed for production and testing. However with the knowledge of this project production of such a rotor should be possible and the maximum speed of the aircraft for 2 EDF's would increase from 185 m/s to 200 m/s. This, without even increasing the EDF efficiency.

8.1 Recommendations

With focus on achieving maximum flight velocity a more accurate prediction of the EDF's power consumption is required. Currently the peak efficiency of the EDF is estimated to be 83% which is high for an axial compressor type machine and seems optimistic. It is therefore suggested that the current and voltage that flow through the engine are measured directly and not only at the start of the power train. This eliminates the uncertainties caused by other components. Since the engine is a three phase brush-less DC engine this should also allow for determining the RPM of the engine which eliminates the need for manual logging of the RPM. Finally, the accuracy of the current model used for the engine efficiency is unknown. It is provided by the manufacturer of the engine without any background information. Therefore it is recommended to test the actual shaft power delivered for varying operating conditions to verify the model, or if it is deemed inaccurate, create a new model.

With regard to the execution of the measurements for the thrust characteristics the following can be recommended.

Firstly, there seems to be a consistency in the uncertainty of the thrust measurements. The uncertainty bounds at the higher velocities are up to 3 times smaller. The cause of this is found in that the measurement error in the actual thrust is consistent independent of the velocity. However

as velocity increases, so does the RPM, which reduces the influence of the error of the thrust in the error of the coefficient of thrust. It is therefore suggested to use a speed of 30 m/s as a reference velocity in future research. Higher speeds would be preferable, but cannot be sustained by the current accelerator.

Secondly, in the current project the EDF is connected to the accelerator in such a way, that the only air flowing through the EDF is that provided by the accelerator. At certain operation points this causes the EDF to act more as a compressor or turbine than an aircraft engine. This is probably the cause for the absence of stall and an over and under pressure at the intake. To prevent this in future use some adaptions to the air accelerator should be made to allow for better simulation of flight conditions. The EDF is placed This is probably the cause for the absence of stall and an over and under pressure at the intake. In actual flight conditions the engine would divert or suck in additional air. To allow this in the setup it is suggested that a connection with the ambient is created right after the diffusor to allow for an additional airflow into or out of the accelerator.

For more accurate predictions of the performance of the EDF 2D and 3D flow phenomena have to be taken into account. An approach for this without direct need of CFD could be streamline curvature correction methods. In this project these have not been investigated, but these could offer a significant accuracy increase over current 1D model.

Bibliography

[1] International Air Transportation Association Annual Review 2018. Technical report, International Air Transportation Association, 2018. 1

[2] Werner R Britsch. Aspect Ratio , and Solidity on Overall Performance of 14 Compressor Middle Stages Aspect Ratio , and Solidity on Overall Performance of 14 Compressor Middle Stages. (September 1979), 1979. 17

[3] R. Coolen. The redesign, manufacturing and testing of an air accelerator for dynamic EDF tests. Technical report, 2019. 2

[4] Marek Darecki and Charles Edelstenne. Flightpath 2050 Europe's vision for aviation: Report of the high level group on aviation research. Technical report, 2011. 1

[5] A. Richard Felix. Summary of 65-series compressor-blade low-speed cascade data by use of the carpet-plotting technique. Technical report, NACA, 1957. 11, 12, 58

[6] H. Cohen G.F.C. Rogers. *Gas turbine theory*. 5th edition, 2001. 4, 5, 12, 15, 16, 41

[7] S.P.W.M. Hoppenreijs. Bachelor Final Project Solar Jet Energy carrier. 2017. 3

[8] ICAO. Resolution A39-2: Consolidated statement of continuing ICAO policies and practices related to environmental protection – Climate change. Technical report, 2016. 1

[9] A.C.F. Janssen. The design, production and qualification of an air acceleration device for EDF dynamic tests. Technical Report June, 2018. 25

[10] R. Jones and D.H. Williams. Effect of Surface Roughness on Characteristics of Aerofoils N.A.C.A. 0012 and R.A.F. 34. Technical report. 18

[11] Rivi Lg, By L Joseph Herrig, James C Emery, and John R Erwin. Systematic Two-Dimensional Cascade Tests of. 1951. 14, 19, 20, 43, 61

[12] Sigrun Matthes, Helmut Ziereis, Florian Linke, Christine Frömming, Katrin Kölker, Volker Grewe, Margarita Vázquez-Navarro, Johannes Hendricks, Jesper Van Manen, Stefan Kaufmann, Katrin Dahlmann, Klaus Gierens, Kai Wicke, Simon Unterstrasser, Ivan Terekhov, Tanja Luchkova, Benjamin Lührs, Simon Rosanka, Malte Niklaß, Martin Plohr, Andreas Minikin, Andreas Zahn, Angela Schmitt, Patrick Jöckel, Ulrich Schumann, Robin Ghosh, Christiane Voigt, Jan Flink, Hiroshi Yamashita, Romy Heller, and Mattia Righi. Mitigating the Climate Impact from Aviation: Achievements and Results of the DLR WeCare Project. Technical Report 3, 2017. 1

[13] NPTEL. Fluid machinery lecture. `https://nptel.ac.in/courses/112104117/chapter_5/4_16.html`. 7

[14] Emma Nygren, Kjell Aleklett, and Mikael Höök. Aviation fuel and future oil production scenarios. *Energy Policy*, 37(10):4003–4010, 2009. 1

[15] Joep Van Oorschot. Design , Production and Testing of a High-Speed Electric Ducted Fan for a Record-Speed Model Airplane. 2018. 1, 2, 3, 6, 7, 8, 9, 10, 11, 20, 42, 46, 47, 51, 52

[16] Jasper Oranje. Schakel Eindproject (SEP) - Propulsion for the Solar Jet. 2016. 3

[17] International Civil Aviation Organisation. Annual Report of the Council 2016. `https://www.icao.int/annual-report-2016/Pages/default.aspx`, url = https://www.icao.int/annual-report-2016/Pages/default.aspx. 1

[18] M Palmer. Propagation of Uncertainty through Mathematical Operations. *MIT School-Wide Modular Program for Fluid Mechanics*, pages 1–7, 2003. 66

[19] Joyce Penner. Aviation and the global atmosphere: a special report of IPCC Working Groups .... (January):373, 1999. 1

[20] Robert D. Blevins. *FORMULAS FOR DYNAMICS, ACOUSTICS AND VIBRATION*. 2015. 34

[21] R Willems. Department of Mechanical Engineering 4WC00 - Bachelor Final Project Team AIR / e Design 2 nd prototype. 2018. 1

[22] Guinness world records. Fastest remote-controlled jet-powered model air- craft (RC). `http://www.guinnessworldrecords.com/world-records/%0Afastest-remote-controlled-jet-powered-model-aircraft-(rc)`. 1

[23] Terry Wright and Philip Gerhart. *Fluid Machinery: Application, Selection, and Design, Second Edition*. 2nd edition, 2009. 8, 57

Appendix A

Design from desired deflection

Designing a cascade from conditions determined in section 2.1 is done via the following procedure. From [23] and rewriting equation 2.2 the difference in tangential velocities can be determined depending on the available input power as follows.

$$P_{in} = \frac{P_{fluid}}{\eta_s} = \dot{m}\frac{T_{01}c_p\left[\left(\frac{p_{03}}{p_{01}}\right)^{\frac{\gamma-1}{\gamma}} - 1\right]}{\eta_s} = \dot{m}(U_{m2}C_{\theta 2} - U_{m1}C_{\theta 1}) \tag{A.1}$$

Than using: $C_{a1} = C_{a2} = C_{a3}$, $U = \omega r$ and $C_{a1} = C_1$ the deflection ϵ is determined. It has to be kept in mind that the Haller ratio for as well the rotor H_{rotor} and the stator H_{stator} should be larger than 0.72. For the rotor H_{rotor} is equal to W_2/W_1 and for the stator H_{stator} is equal to C_3/C_2.

Using a different set of carpet plots one can now determine the required camber and and stagger angle (via the angle of attack) from the air inflow angle, required deflection and solidity, see Appendix B. With this known one can use the carpet plot as described above to determine the off-performance deflection.

Appendix B

Digitized NACA 65- carpet plots

Shown are projections of the digitized carpet plots. Markers are added as examples. These examples are arbitrary. Data originates from [5]. Digitazation was done as follows: Firstly the carpet plots where converted to a binary image using edge detection in Matlab. Consequently a script converted the binary image to lines which can be plotted. Finally an algorithm was written that performs the interpolation.

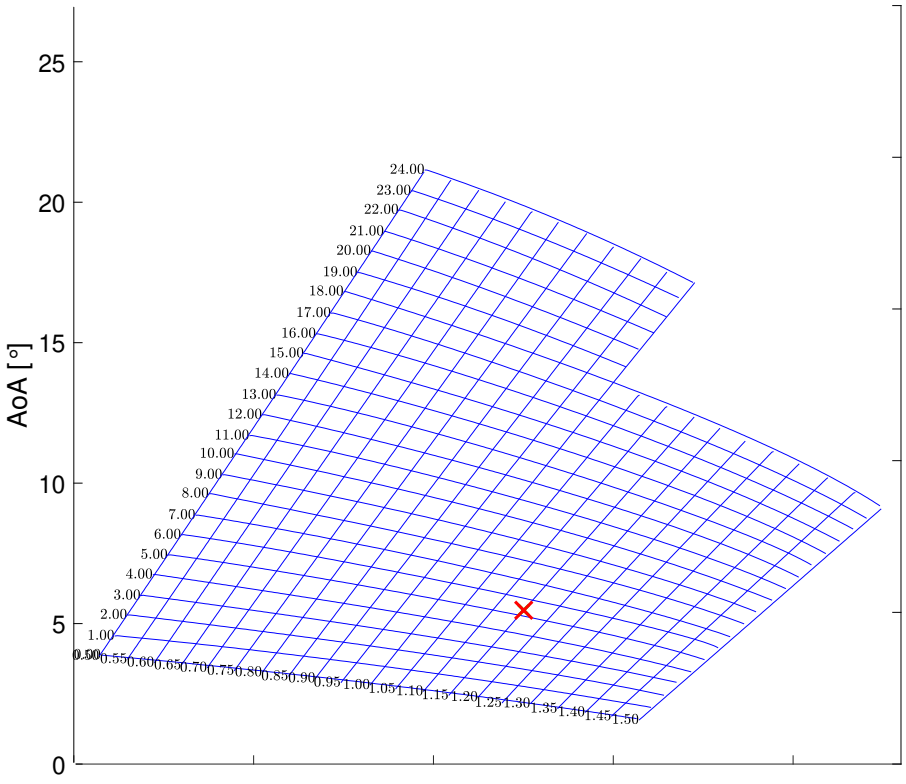

Figure B.1: Visualisation of the digital carpet plot for determining the angle of attack from the solidity σ and camber C_{l0}. The example indicated by the marker gives a value $A0A = 6.6°$ for $C_{l0} = 5.2$ and $\sigma = 1.15°$

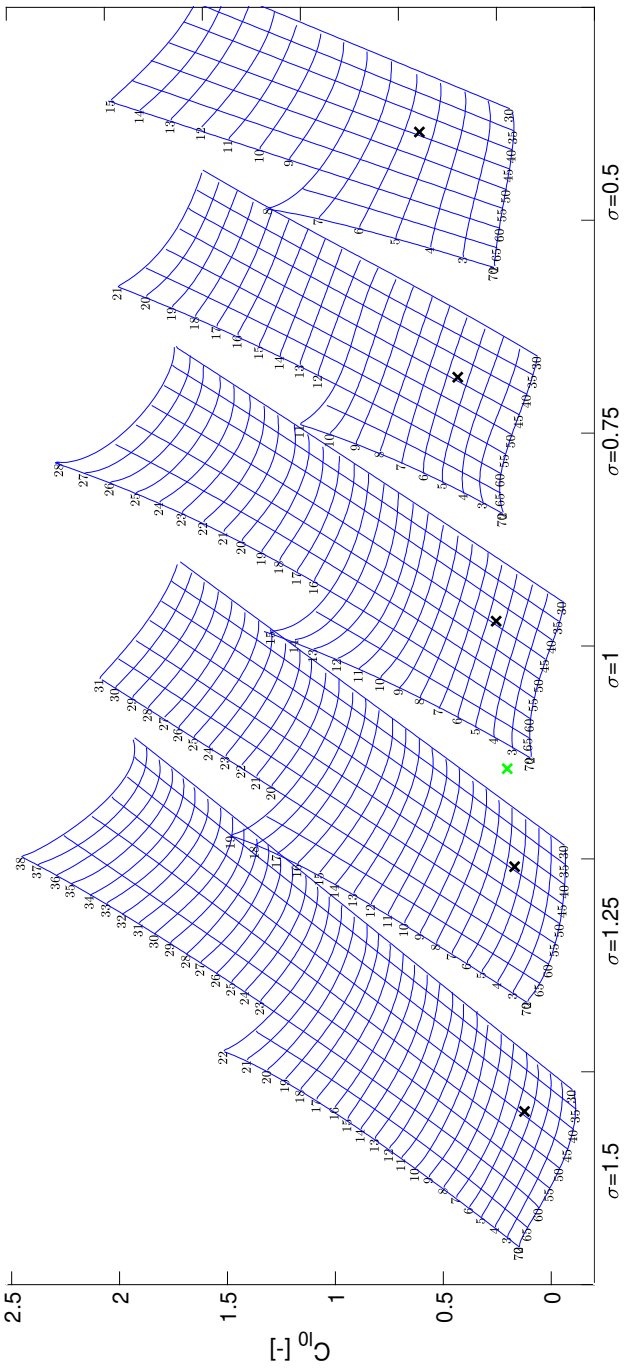

Figure B.2: Visualisation of the digital carpet plot for determining the camber C_{l0} from the solidity σ, required deflection ϵ and air inflow angle β_1. The example indicated by the markers give a value $C_{l0} = 0.18$ for $\sigma = 1.15$, $\epsilon = 5.5°$ and $\beta_1 = 44.2°$

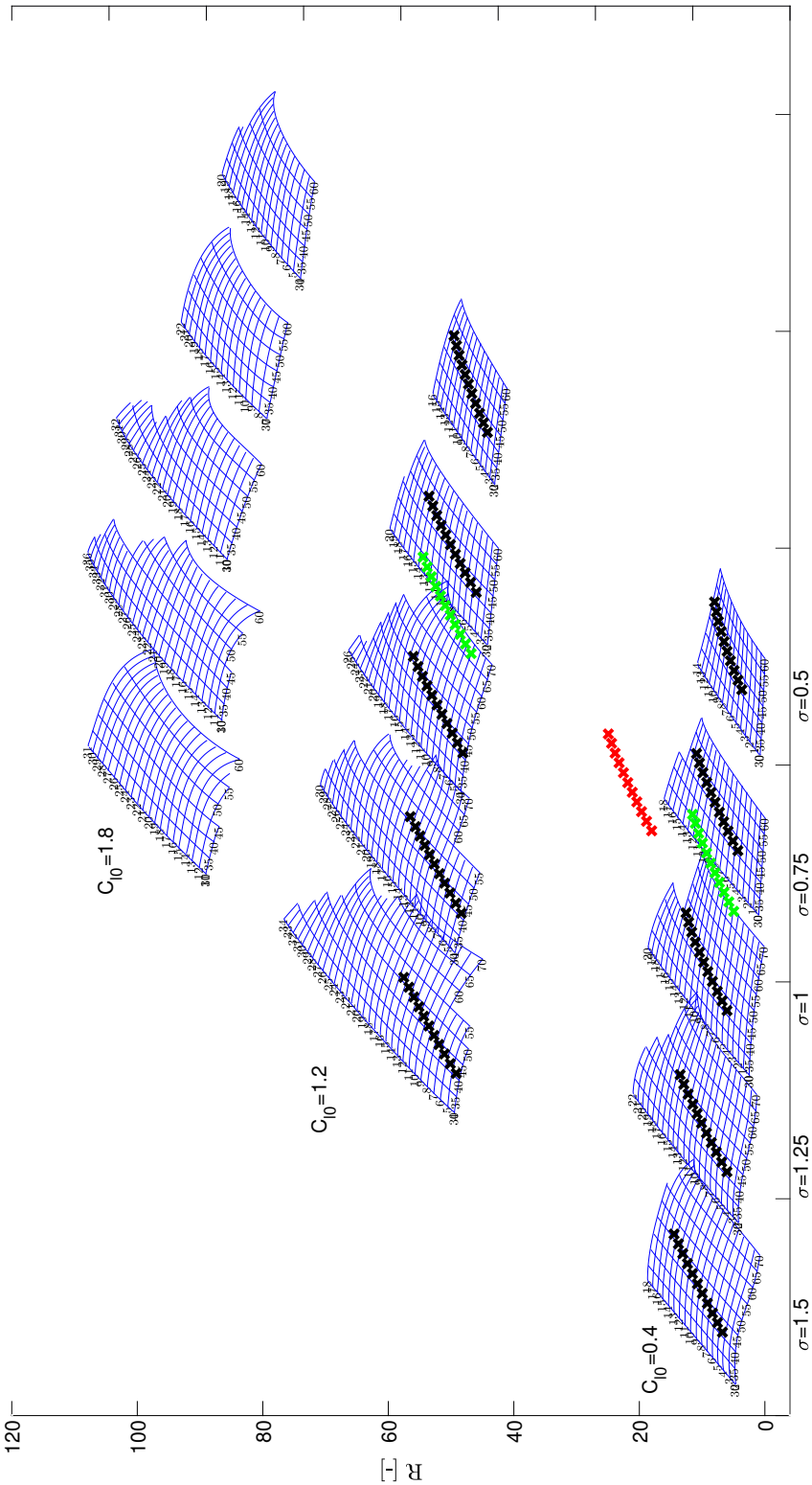

Figure B.3: Visualisation of the digital carpet plot for determining the R value that via equation 2.16 can be converted to a deflection angle η. As input it requires the solidity σ, camber C_{l0}, angle of attack AoA and air inflow angle β_1. The example indicated by the markers are for $\sigma = 0.7$, $C_{l0} = 1.03$, $AoA = 7° - 17°$ and $\beta_1 = 26.6° - 36.6°$

Appendix C

Overview of available test data on the coefficient of drag C_{Dp}

CASCADE COMBINATIONS TESTED

σ	β (deg)			
	30	45	60	70
0.50		65-410 65-(12)10 65-(18)10	65-410 65-(12)10 65-(18)10	
.75		65-410 65-(12)10 65-(18)10	65-410 65-(12)10 65-(18)10	
1.00	65-010 65-410 65-810 65-(12)10 65-(15)10 65-(18)10	65-010 65-410 65-810 65-(12)10 65-(15)10 65-(18)10 65-(21)10 65-(24)10 65-(27)10	65-010 65-410 65-810 65-(12)10 65-(15)10 65-(18)10 65-(21)10	65-010 65-410 65-810 65-(12)10 [a]65-(15)10
1.25	65-410 65-(12)10 65-(18)10	65-410 65-(12)10 65-(18)10	65-410 65-(12)10 65-(18)10	65-410 65-810 65-(12)10 65-(15)10
1.50	65-010 65-410 65-810 65-(12)10 65-(15)10 65-(18)10	65-010 65-410 65-810 65-(12)10 65-(15)10 65-(18)10 65-(21)10 65-(24)10	65-010 65-410 65-810 65-(12)10 65-(15)10 65-(18)10 65-(21)10 65-(24)10	65-010 65-410 65-810 65-(12)10 65-(15)10

[a]No design point was obtained for this combination.

NACA

Figure C.1: Data of the tested cascades in [11]. Table adapted from [11]

Appendix D

Rotor design specifics

This appendix contains the tables showing the detailed geometrical properties of the rotor designs. Also the measured performance of rotor 4 is given in section D.3. The specifications of rotor 1 are already given in table 2.1. The same holds for the stator vanes, see table 2.2.

D.1 Rotor 2

	Non variable parameters				Variable angles at the design point		
Section No.	r [mm]	$\sigma[-]$	λ [°]	$C_{l0}[-]$	β_1[°]	ϵ [°]	AoA [°]
1	30	1.897	19.6	1.03	32.3	21.1	12.7
2	38	1.498	29.5	0.75	38.7	14.1	9.5
3	46	1.237	36.7	0.65	44.2	9.7	7.5
4	54	1.054	42.5	0.56	48.7	6.8	6.2
5	62	0.918	47.4	0.47	52.6	4.9	5.2

Table D.1: Rotor blade section design parameters of rotor 2

D.2 Rotor 3

	Non variable parameters				Variable angles at the design point		
Section No.	r [mm]	$\sigma[-]$	λ [°]	$C_{l0}[-]$	β_1[°]	ϵ [°]	AoA [°]
1	30	0.699	19.6	1.03	32.3	21.1	12.7
2	38	0.552	29.5	0.75	38.7	14.1	9.5
3	46	0.456	36.7	0.65	44.2	9.7	7.5
4	54	0.388	42.5	0.56	48.7	6.8	6.2
5	62	0.334	47.4	0.47	52.6	4.9	5.2

Table D.2: Rotor blade section design parameters of rotor 3

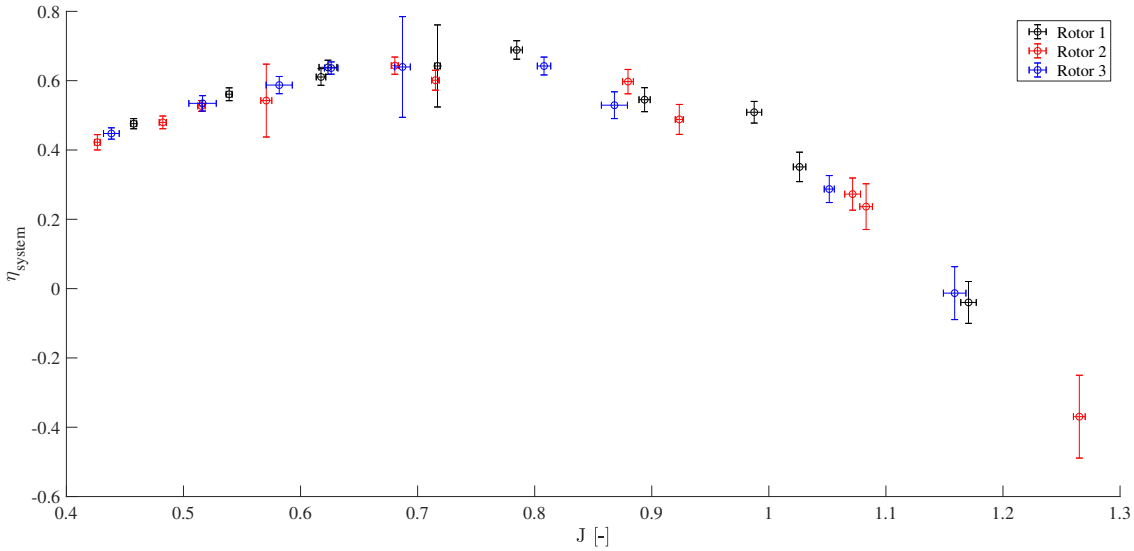

Figure D.1: The system efficiency vs the advance ratio. Data for rotor 1 from run 41 and 42. Data for rotor 2 from run 46 and 47. Data for rotor 3 from run 69 and 70

D.3 Rotor 4

The geometrical properties of rotor 4 are identical to that of rotor 1, therefore see table 2.1. Figure D.2 shows the measured performance of rotor 1 versus the measured performance of rotor 4.

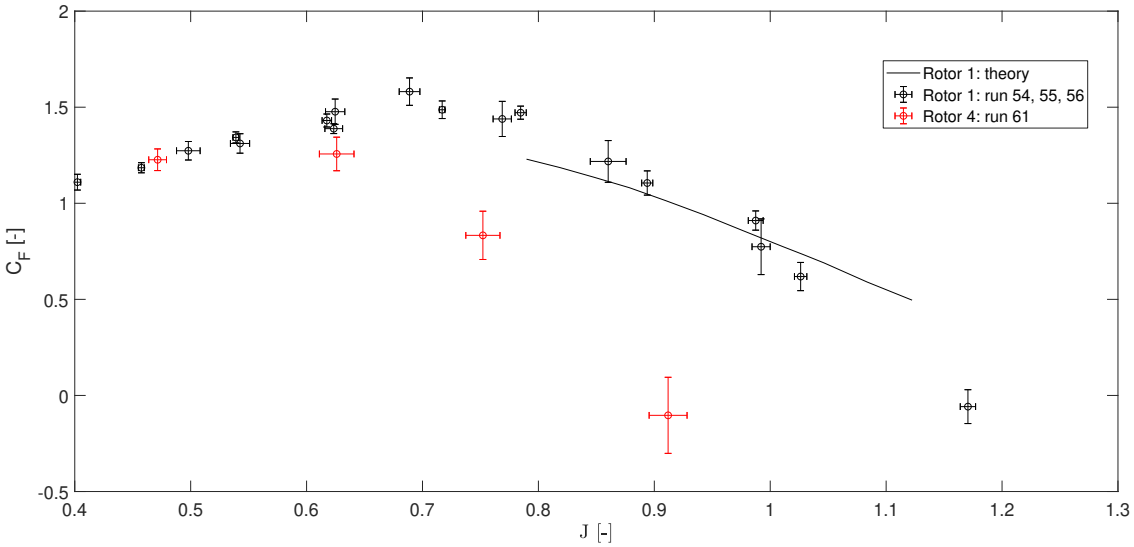

Figure D.2: The predicted and the measured thrust coefficient versus the advance ratio for rotor 1 and rotor 4. Data for rotor 1 from run 40, 41 and 42. Data for rotor 4 from run 61.

Rotor 4 performs significantly worse than rotor 1. This is most probably not the result of the rotor blades being smoother, but because the process has not been executed correctly. The coating is manually applied afterwards. From inspection of the rotor it can be concluded that the vernis did not evenly spread over the cascade shapes. This both deformed the cascade shapes, mainly at the trailing edge, and resulted in an inbalanced rotor.

D.4 Rotor 5

The geometrical properties of rotor 5 are identical to that of rotor 1, therefore see table 2.1.

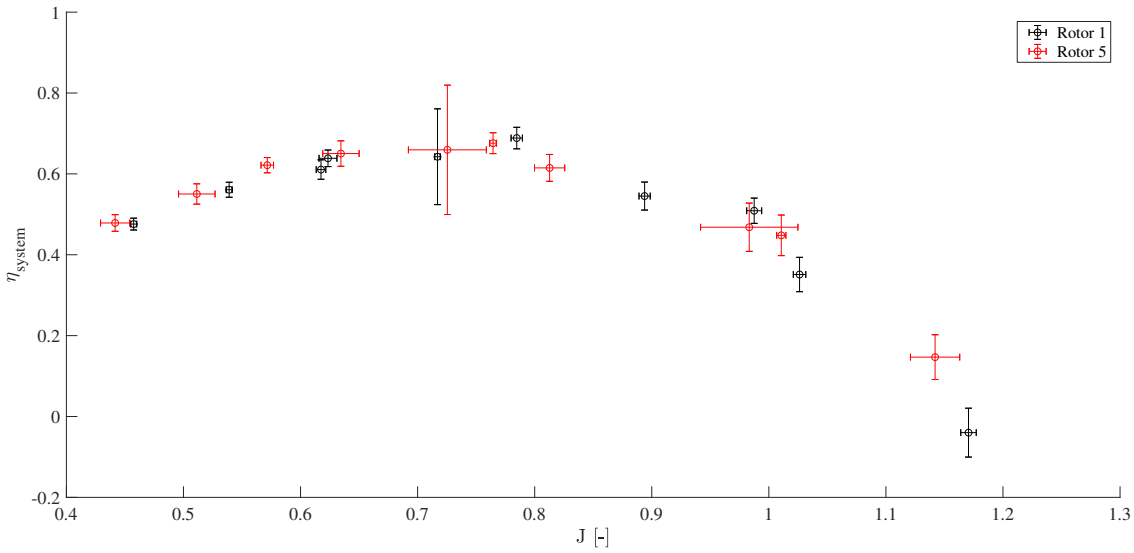

Figure D.3: The system efficiency vs the advance ratio. Data for rotor 1 from run 41 and 42. Data for rotor 5 from run 63 and 64.

D.5 Rotor 6

	Non variable parameters				Variable angles at the design point		
Section No.	r [mm]	$\sigma[-]$	λ [°]	$C_{l0}[-]$	β_1[°]	ϵ [°]	AoA [°]
1	30	1.297	17.1	1.03	32.3	23.2	15.3
2	38	1.024	27.0	0.75	38.7	18.7	11.8
3	46	0.845	34.2	0.65	44.2	15.6	10.1
4	54	0.720	40.1	0.56	48.7	13.4	8.8
5	62	0.627	44.9	0.47	52.6	11.7	7.6

Table D.3: Rotor blade section design parameters of rotor 6

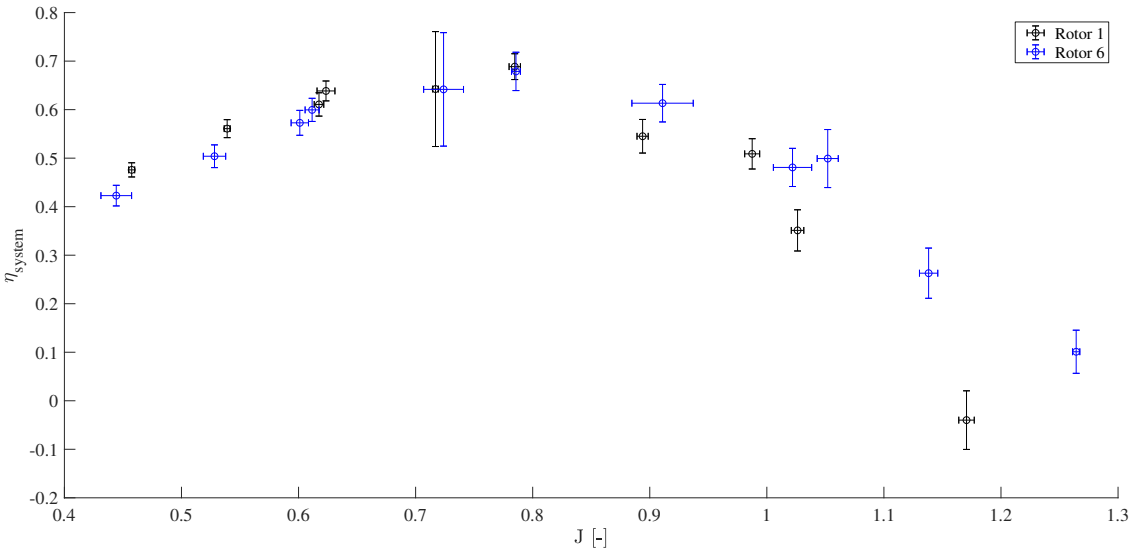

Figure D.4: The system efficiency vs the advance ratio. Data for rotor 1 from run 41 and 42. Data for rotor 2 from run 66 and 67.

Appendix E

Error propagation

The uncertainty of the measured quantities is acquired by multiplying the standard deviation of a set of samples with the proper student-t factor for a 68.2% confidence interval. For a large number of samples this converges to a single standard deviation of the sample set. The propagation of the uncertainty is calculated with [18]:

$$\delta R = \sqrt{\left(\frac{\partial R}{\partial X}\delta X\right)^2 + \left(\frac{\partial R}{\partial Y}\delta Y\right)^2 + ...} \tag{E.1}$$

Appendix F

LMT 3380/7 characteristics

Figure F.1 shows the efficiency of the LMT 3380/7 electric motor for different input voltages versus the percentage of the maximum input power of the motor. Data obtained from [**?**].

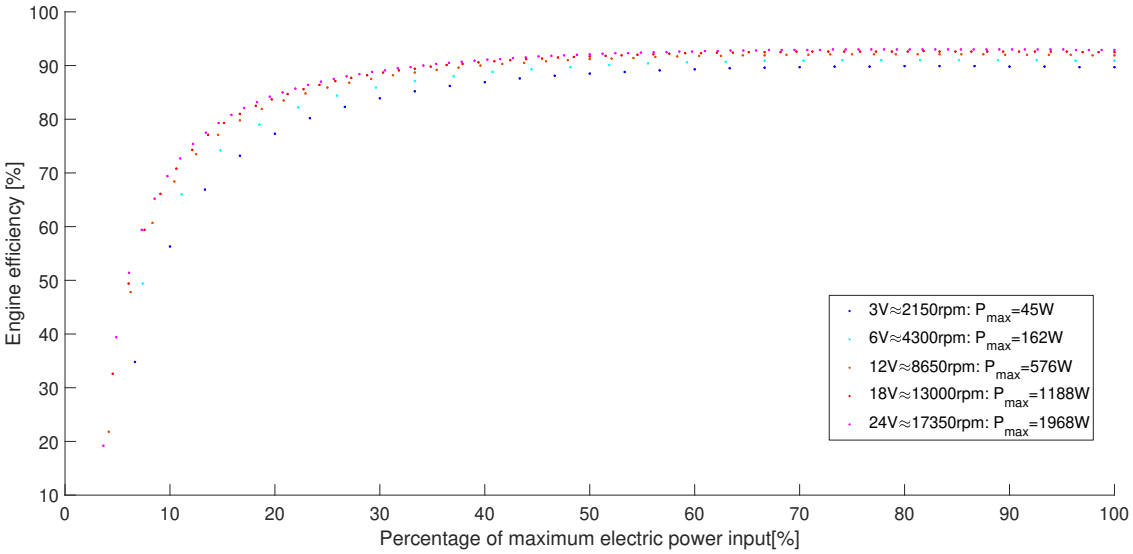

Figure F.1: Electric motor efficiency versus the percentage of the maximum power output

Figure F.2 shows the maximum power the LMT 3380/7 can deliver at varying rotational speeds.

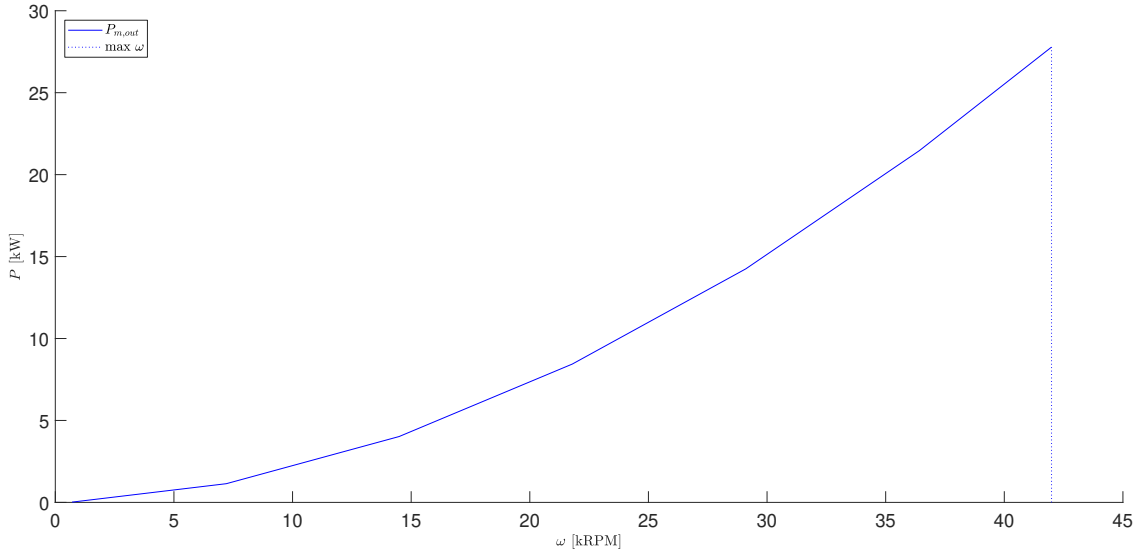

Figure F.2: Maximum power output of the electric engine versus the rotational speed

Appendix G

Pressure and velocity relations between V1 and V2/V3

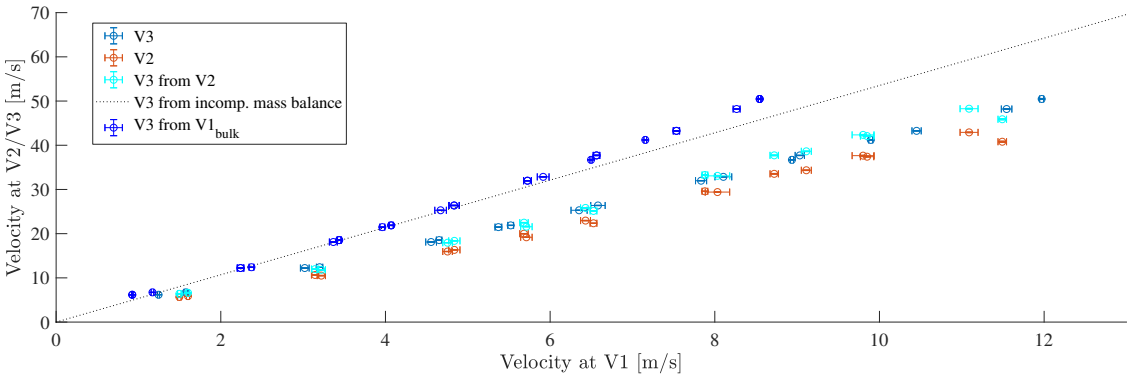

Figure G.1: Relation between the velocity measured at V1 and V2/V3. Using the relation between the surfaces A2 and A3 one can achieve V1 vs V3 from V1 vs V2. The dotted line is V1 vs V3 according to in-compressible mass balance.

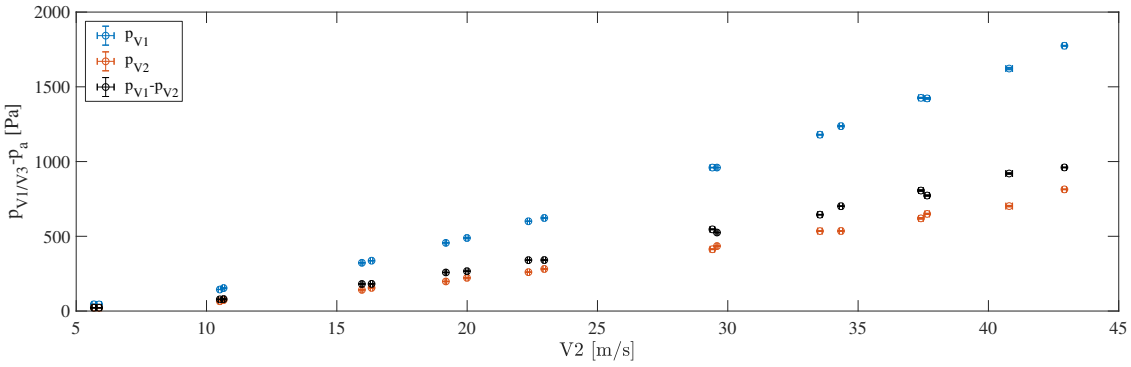

Figure G.2: Difference between static pressure at V1 and V2 with the atmospheric pressure for velocity calibration run 75 and 78. Atmospheric pressure is 995 hPa

The difference in density between V1 and V2 can be calculated using the ideal gas law. During the calibration measurements the maximum difference in densities is:

$$\frac{p_a + p_{V1}}{R_{air} T_{V1}} - \frac{p_a + p_{V2}}{R_{air} T_{V2}} = \frac{9.95e4 + 1775}{286.9 \cdot 295} - \frac{9.95e4 + 813}{286.9 \cdot 295} = 1.20 - 1.19 \tag{G.1}$$

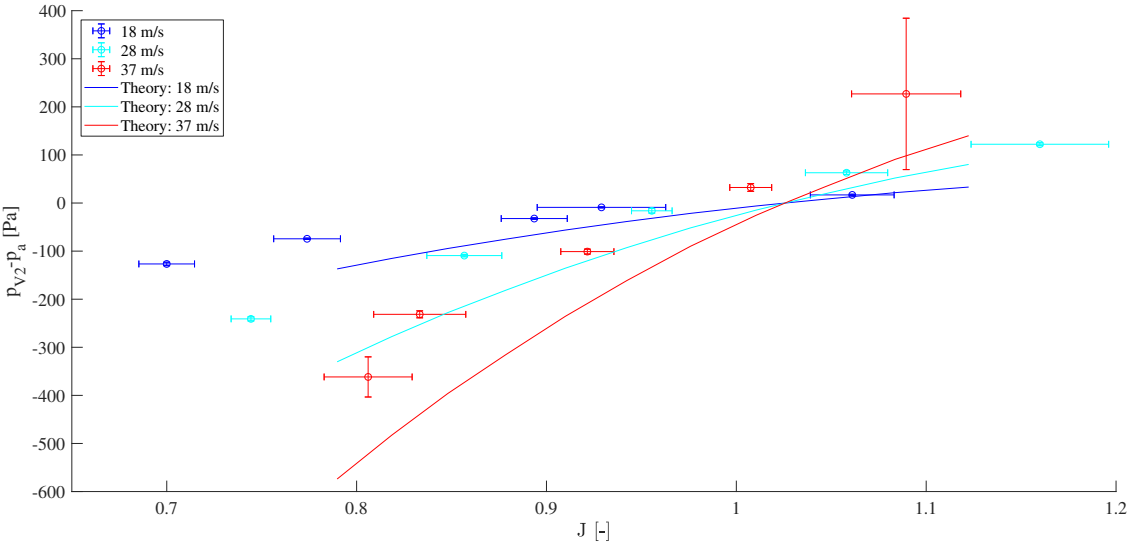

Figure G.3: Theoretical pressure difference required at intake for matching mass flow rates of the accelerator and the nozzle, vs the measured pressure difference at the intake/V2.

Appendix H

Calibration of the force sensor

Figure H.1 shows the result of the calibration of the loadcell.

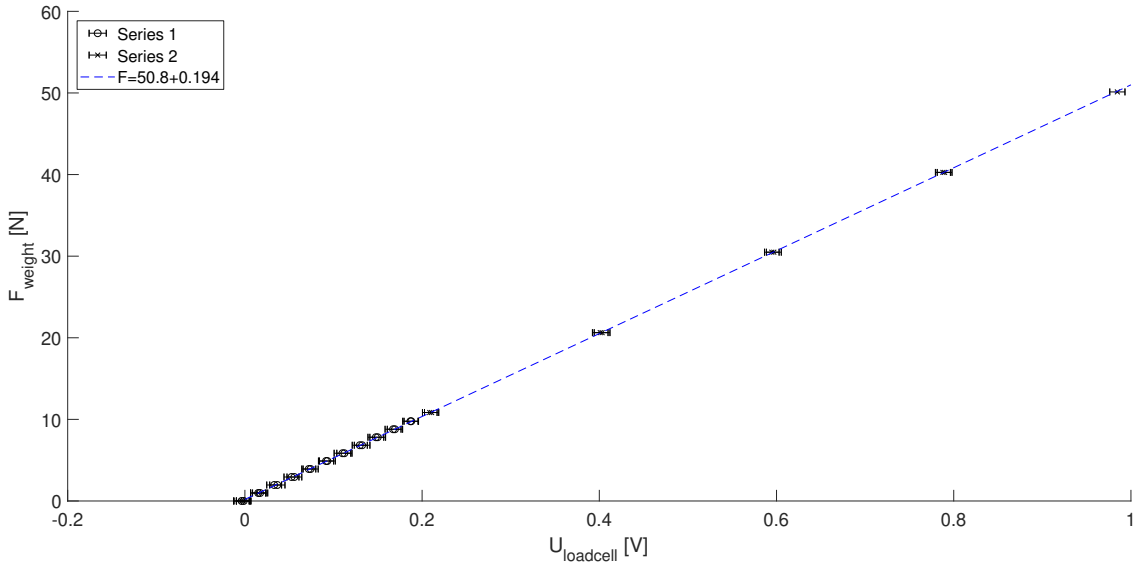

Figure H.1: Output voltage of the loadcell versus the weight attached in Newtons

Appendix I

Overview of measurement runs (Runlog)

Details of the measurements can be found in a log file. From this file the details (Measurement type, used equipment, date, position of senors, etc.) for a certain run ID can be retrieved. Shown in table I.1 are the descriptions (in summarized form) of the runs from which data is presented in this thesis.

ID	Type	Rotor	velocity target [m/s]	Comment	Date
0.5	Dynamic	1	20	Old setup	X
0.6	Dynamic	1	40	Old setup	X
0.7	Dynamic	1	50	Old setup	X
40	Dynamic	1	20		23-11-2018
41	Dynamic	1	40		23-11-2018
42	Dynamic	1	30		23-11-2018
43	Camera	1	5-45	Stationary rotor, 5000M GO	30-11-2018
45	Dynamic	2	20		10-12-2018
46	Dynamic	2	40		10-12-2018
47	Dynamic	2	30		10-12-2018
48	Camera	1	5-40	Stationary rotor, PCO 1200hs	14-12-2018
61	Dynamic	4	20		23-01-2019
62	Dynamic	5	20		18-03-2019
63	Dynamic	5	40		18-03-2019
64	Dynamic	5	30		18-03-2019
65	Dynamic	6	20		19-03-2019
66	Dynamic	6	40		19-03-2019
67	Dynamic	6	30		19-03-2019
68	Dynamic	3	20		02-04-2019
69	Dynamic	3	40		02-04-2019
70	Dynamic	3	30		02-04-2019

Table I.1